Energetic Consideration and Structural Characterization of Twinning in Nanowires

Chun-Hsien Wu

Dissertation submitted to the faculty of the
Virginia Polytechnic Institute and State University
in partial fulfillment of the requirements for the degree of

Doctor of Philosophy
in
Materials Science and Engineering

Mitsuhiro Murayama
William T. Reynolds Jr.
Sean Corcoran
William A. Soffa

April, 5th 2013
Blacksburg, Virginia

Keywords: twinning, twinning superlattice, nanowires, 3D microscopy

Energetic Consideration and Structural Characterization of Twinning in Nanowires

Chun-Hsien Wu

Abstract

Twins are a pair of adjoining crystal grains related to each other by a special symmetry. They are frequently observed in bulk materials and nanomaterials. The formation of twins is an important topic in materials science and engineering because it affects material behaviors such as plastic deformation of metals, yield strength, and band gap energy in nanoscale semiconductors. Because of these unique phenomena and properties that the twinning can bring to the materials, it is of interest to investigate the formation of twins. Our primary objective in this dissertation is to study twinning in nanowires.

Both gold and platinum <111> oriented nanowires were fabricated by similar solution-phase chemical synthesis methods. High-resolution transmission electron microscopy and electron diffraction patterns were carried out to analyze the structures of the nanowires. Nanodiffraction was used to demonstrate twinning is a general structural feature of the growth of gold nanowires growing in a <111> direction. A model was proposed to explain the conditions under which twinning is energetically favored during nanowire growth. The model, which is based on a maximum rate hypothesis, considers the nanowire geometry and the relative surface and stacking fault energies and predicts twins should appear in gold nanowires but not in platinum nanowires, in agreement with experimental observations.

During the structural characterization of gold nanowires, our interest is to

resolve 3D structure of twinning. However, the structure of twinning in gold nanowires is very fine and the average spacing between twin boundaries is only 0.57nm (+/- 0.38 nm); therefore, regular 3D electron microscopy technique is unable to reconstruct these defected structures. Here we present a stereo vision technique to reconstruct 3D atomic non-periodic structures containing defects. The technique employs intrinsic atomic planes as epipolar planes to achieve the alignment accuracy needed to reconstruct a crystal with atomic resolution. We apply it to determine the 3D geometry and atomic arrangements of twinning in gold nanowire.

In addition, an iterated cross-correlation algorithm was developed to analyze electron diffraction fully automatically to facilitate structural analysis of nanowires. A time-temperature-transformation diagram of platinum nanowires in chemical synthesis was determined to help optimize the fabrication process of the nanowires.

Acknowledgements

I would like to thank my advisor, Dr. Mitsuhiro Murayama, for his guidance and funding support. During my pursuit of PhD degree, he generously supports me to attend TEM training, international conferences and oversea research collaboration. These are valuable experiences that I never had before; therefore, I really appreciate for his support. Most important of all, he taught me the way of reasoning in science research so I can identify important problems in materials science research. This skill is extreme valuable asset for my future carrier. At the same time, I would also like to thank my co-advisor, Dr. William T. Reynolds Jr., for his mentor in learning, researching and self-establishing. Without him, I would not have opportunity to establish myself in the PhD program and continue improving my science research skills. During my years in Virginia Tech, I feel grateful to have both Dr. Murayama and Dr. Reynolds to instruct me. It is my honor to be their student. They taught me not only the knowledge of science but also the way of doing research.

Besides my thanks to my advisor and my co-advisor, during my years in Virginia Tech there are many other people who help me and guide me throughout the PhD program. I want to give my special thanks to Dr. Deborah M. Aruguete for her training in chemical synthesis and guidance in scientific writing. Without her instruction, I could not fabricate nanowires for my research. I want to thank Dr. Kazuhisa Sato for his help in tomography data acquisition and his generous care when I was in Tohoku University. I want to thank Yuan Zhou for his collaboration in fabrication of barium titanate columnar structures. Also, I want to thank my committee members Dr. William A. Soffa and Dr. Sean Corcoran for their valuable comments in my qualifying exam and preliminary exam. I wish to thank Dr. Hochella

for his generosity in allowing me to use his chemical synthesis equipment and chemical lab. Moreover, I want to thank Dr. Niven Monsegue for his help in tomography reconstruction and Ms. Hong Pang for her assistant in chemical synthesis of platinum nanowires. At last, I truly appreciate the funding support from Virginia Tech ICTAS junior faculty award and the facility in NCFL.

Table of Contents

List of Figures

Chapter 1 Introduction

Chapter 2 Twinning in <111>-Oriented Ultrathin Gold Nanowires: Structural Characterization and Energetic

Chapter 3 Three-Dimensional Atomic Imaging through Stereo Vision

Chapter 6 TEM Characterization of Pulsed Laser Deposition $BaTiO_3$ Film on Platinized Silicon

List of Tables

Chapter 1 Introduction

1.1 Dissertation Structure

The structure of this dissertation is composed as follows.

1. Chapter one describes the background and motivation of this PhD dissertation research.
2. Chapter two focuses on studying the formation mechanism of twinning in <111> oriented nanowires fabricated by solution-phase chemical synthesis. Several characterization techniques such as bright field imaging, HRTEM and parallel nanobeam diffraction [1-4] were applied to resolve the atomic structure of gold and platinum nanowires. A geometrical model [5] was proposed to elucidate formation of twinning and twinning superlattice in gold nanowires.[6]
3. Chapter three shows a novel development in 3D transmission electron microscopy technique [7] to resolve three-dimensional atomic structure of twinning and defected structure in <111> oriented gold nanowires. The technical development of electron tomography reconstruction allows us to locate individual atom positions thus the determination factor of the spatial resolution of reconstructed tomogram simply depends on the resolution of imaging device. The result demonstrates that it can archive beyond the current resolution limit of 2.4 angstrom.[8]
4. Chapter four introduces a newly developed software tool, which can facilitate the diffraction analysis of electron diffraction patterns taken from nanowires. A new iterated cross correlation algorithm has been developed to enable software to detect and analyze diffraction spots automatically. This chapter has been accepted as full length journal article in Ultramicroscopy.[9]
5. Chapter five presents an investigation of morphology control of platinum nanowires by variation of reaction time and temperature in solution-phase chemical synthesis.[10] A series of experiments to optimize both reaction time and temperature has been made to enable the fabrication of <111> oriented platinum nanowires with high aspect ratio.

6. Chapter six focuses on studying the formation of twinning and the control of growth orientation in barium titinate columnar structures grown by PLD. This attempts to examine whether a structural defect in both pure metallic and metallic oxide nanostructure has a similar role on the microstructure formation. This work was in collaboration with a group studying thin film deposition. My role in the investigation was to characterize the defected structure in barium titanate thin film.
7. Chapter seven is the summary of all the research projects pursued in this dissertation.

References were listed in the end of each of chapter for ease of organization.

1.2 Nanomaterials

Nanomaterials which are defined as materials with one dimensional or multi-dimensional size range from 1nm to 100nm are my field of interests in this dissertation. They are of interests in science and engineering research because their small sizes allow miniaturization of various engineering devices and they possess unique properties rather than their bulk counterpart.[8] Most of these unique properties are considered to be due to their size effect.[1, 8] When the size of a material reaches nanometer scale, the material has high surface to volume ratio and this results in high number of dangling bonds appeared on the surface of the nanomaterial in relative small volume. The large number of dangling bonds may destabilize the structure of a nanomaterial and changes its physical property such as phase transformation temperature. For example, the melting temperature of a nanoparticle is often lower than its bulk counterpart [8] and this lowering of melting temperature may limit its application in engineering and technology. Therefore I am interested in the factors that contribute to the unique properties of nanomaterials. One well-known factor is size effect which has already been studied extensively. In this dissertation, I focus on studying the influence of defected structure in nanomaterials.[11]

Nanomaterials consists wide variety of morphology such as nanospheres, nanocubes, nanowires, nanodendrites, etc. Here I choose nanowires which have unique optical, electronic and mechanical properties as my materials of interest.

1.3 Nanowires

Nanowires are one-dimensional nanomaterials. The two-dimensional quantum well confinement in nanowires results in unique electronic property and optical property of nanowires.[12] For example, the two-dimensional quantum well in metallic nanowires can restrain the movement of electrons in only one dimension. This makes the metallic nanowires a perfect candidate to serve as conducting media in nanoelectronic device. Furthermore, the electron density of states and band gap energy are also affected by two-dimensional quantum well; thus, the optoelectric property such as optical absorption range [13] and band gap energy in semiconductor nanowire can be tuned by adjusting the diameter of nanowires.[14, 15] Besides their unique electronic and optical properties, nanowires can also have high Young's modulus.[16] This leads to potential application in mechanical enhancement in composite materials.

1.3.1 Fabrication of Nanowires

To study defected structure in nanowires, fabrication of nanowires is a necessity. In last decade, many fabrication techniques of nanowires were developed. Generally they can be classified into two categories: chemical synthesis and physical vapor deposition. In chemical synthesis, solution-phase chemical synthesis is a standard technique commonly used to fabricate inorganic nanowires, especially metallic nanowires. On the other hand, semiconductor and ceramic nanowires are commonly fabricated through physical vapor deposition system. Here I show two fabrication techniques that were applied to fabricate nanowires in this dissertation. One is solution-phase chemical synthesis and the other is pulsed laser deposition.

1.3.1.1 Solution-Phase Chemical Synthesis

In chemistry society, solution-phase chemical synthesis is a standard method to fabricate inorganic nanowires. A general setup of solution-phase chemical synthesis is shown in Figure 1.1. The benefit of solution-phase chemical synthesis is its superior control over

morphology, monodispersity and self-assembly of nanocrystals.[17, 18] During a general chemical synthesis, it is typical to have precursors, solvent, reducing agent and surfactant in a reaction flask. Each individual element inside the reaction flask has its own implication. The precursors serve as source materials for nanowire growth. The solvent is applied to suspend the nanowires. The surfactant is utilized to control the morphology of nanoparticles to grow nanowires.[19] At last, the reducing agent is employed to reduce metallic ions to form nanowires. To prevent any oxidation of nanowires, a Schlenk line is typically used to enable nanowires to be chemically synthesized under inert gas condition.

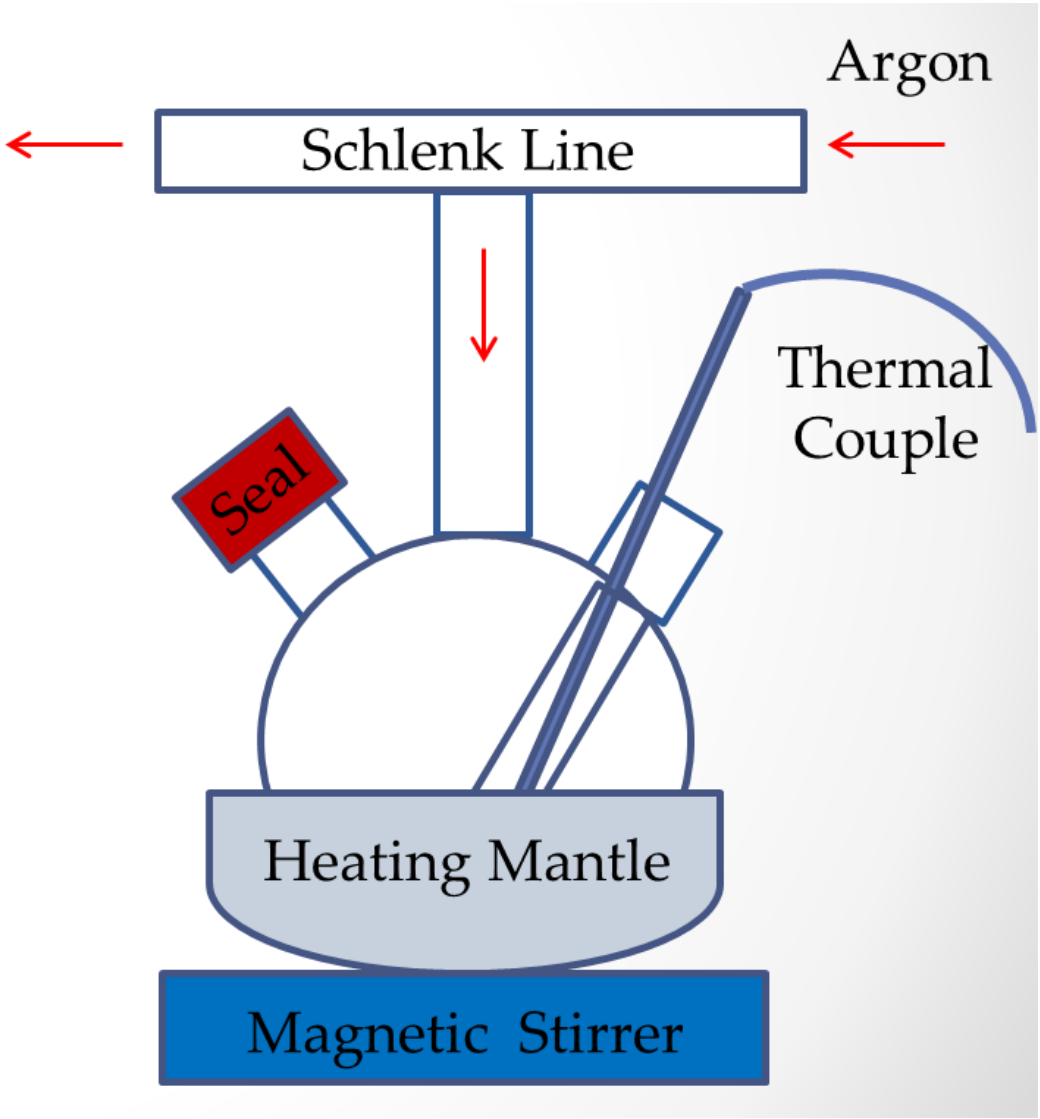

Figure 1.1: Illustration of solution-phase chemical synthesis setup.

1.3.1.2 Pulsed Laser Deposition

Pulsed laser deposition (PLD) [20-22] is one of physical vapor deposition techniques generally applied to fabricate thin film, semiconductor device and nanostructured material. A general setup of PLD system is shown in Figure 1.2. In PLD system, a high power pulsed laser is focused to hit target material and generate a plasma plume which deposits material onto a substrate. During the deposition there are several parameters which can be adjusted to tune the morphology and the microstructure of deposited products. The thickness of thin film and size of nanoparticles can be controlled by the number of laser ablation pulses. The chemical composition of the product can be tuned by the target material. The quality of deposited product is affected by the atmosphere in the system chamber. The morphology of nanoparticles can be engineered by lithography or substrate temperature.[23, 24] At last, the crystal orientation of deposited thin film can be controlled by epitaxial growth from the substrate.[25]

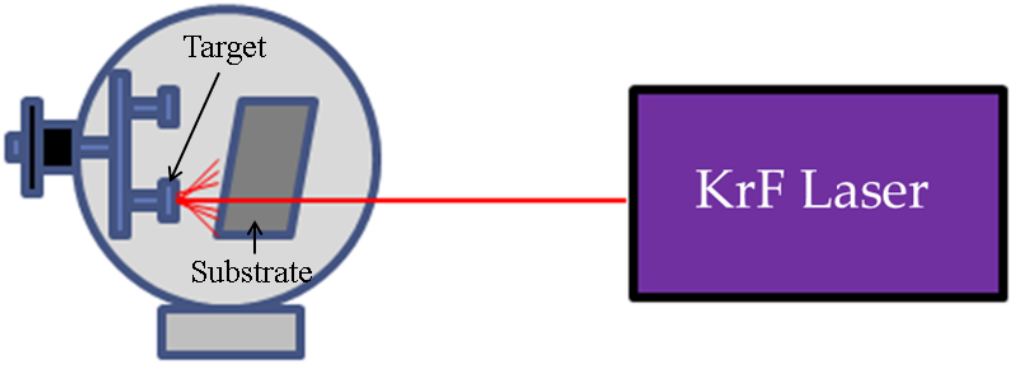

Figure 1.2: Illustration of pulsed laser deposition setup.

1.3.2 Methods to Characterize Nanowires

To characterize defected structure in nanowires, characterization methods which are capable of resolving structural feature less than 100nm in size is needed. A typical transmission electron microscope (TEM) can have sub-nanometer resolution; therefore, TEM

is extensively utilized to characterization nanostructure and morphology of nanomaterials. Here are several TEM techniques which were used and applied in this dissertation: TEM bright field imaging, high resolution transmission electron microscopy (HRTEM), parallel nanobeam diffraction[1-4] and electron tomography[7]. The application of individual technique is described as follows.

1.3.2.1 TEM Bright-Field Imaging

A typical technique to resolve the morphology of nanoparticles is conventional bright field imaging in TEM. During the imaging, the objective aperture is inserted to block diffracted beam and then only allows center beam to pass through the aperture. This method can generate higher diffraction contrast in the acquired images and reveal the morphology of nanoparticles. Figure 1.3 is a bright-field image of gold nanowires.

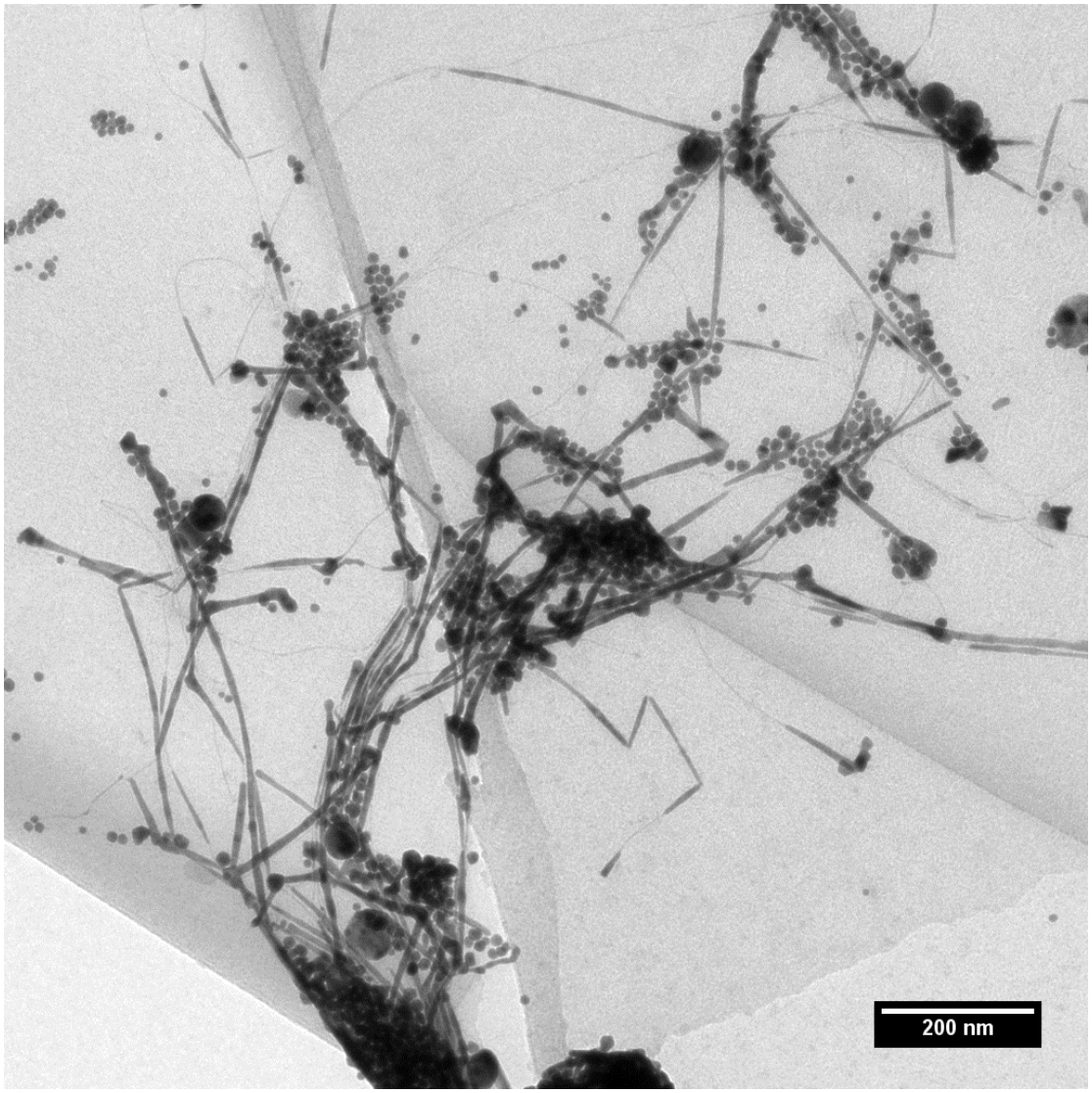

Figure 1.3: TEM bright field imaging of gold nanowires.

1.3.2.2 HRTEM

HRTEM is a powerful technique to analyze atomic structure of nanoparticle. During the imaging, the objective aperture is extracted from the back focal plane of the TEM to enable the center beam and diffracted beam to interfere and generate phase contrast. The phase contrast can produce lattice fringe from the atomic structure of a specimen as shown in Figure 1.4. By analyzing the lattice fringe, the atomic structure of nanoparticles can be revealed.

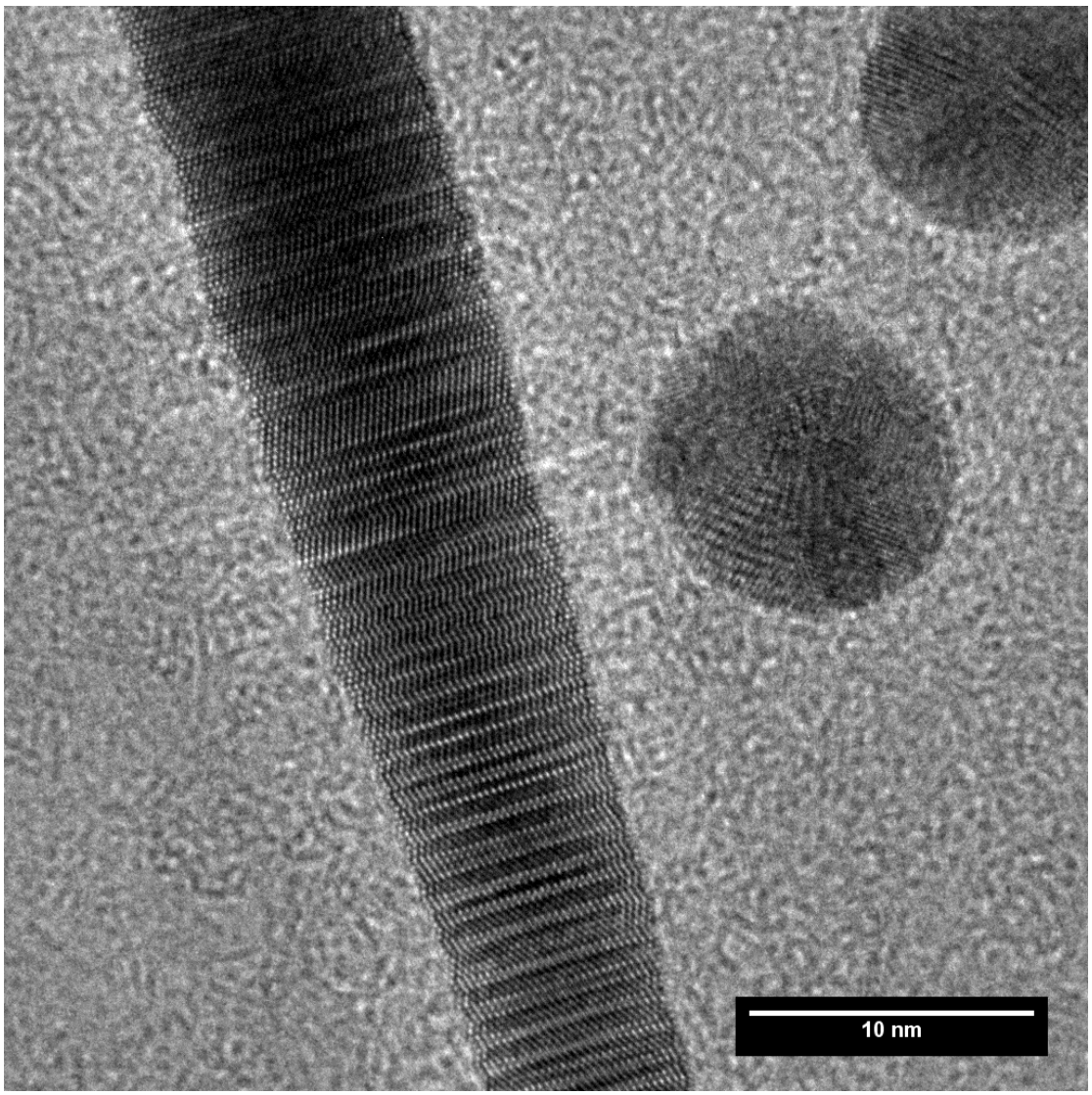

Figure 1.4: Lattice fringe of a gold nanowire taken by HRTEM.

1.3.2.3 Parallel Nanobeam Diffraction

Traditional nanobeam diffraction utilized a non-parallel beam focused on a specimen by condenser lens in TEM mode to generate convergent beam electron diffraction pattern. The diffraction pattern taken in this method would have reflection spots in disk shape rather than in regular spot shape. Therefore it is more difficult to interpret the data.

In contrast, the parallel nanobeam diffraction [1-4] applied in this dissertation is a special setup in scanning transmission electron microscopy (STEM) mode to allow parallel electron beam with spot size of approximately 3nm in diameter scanning over the specimen. Simply speaking, the parallel nanobeam diffraction technique can be considered as selected

area diffraction pattern taken from 3nm spot. Figure 1.5 shows a diffraction pattern taken by parallel nanobeam diffraction from a copper gold nanoparticle indicated by a arrow. With this parallel nanobeam, the structure of individual nanoparticle can be easily analyzed. Besides its benefit in structure analysis, the technique itself is also extremely efficient. One hundred electron diffraction patterns can be acquired within two minutes of beam time in STEM mode.

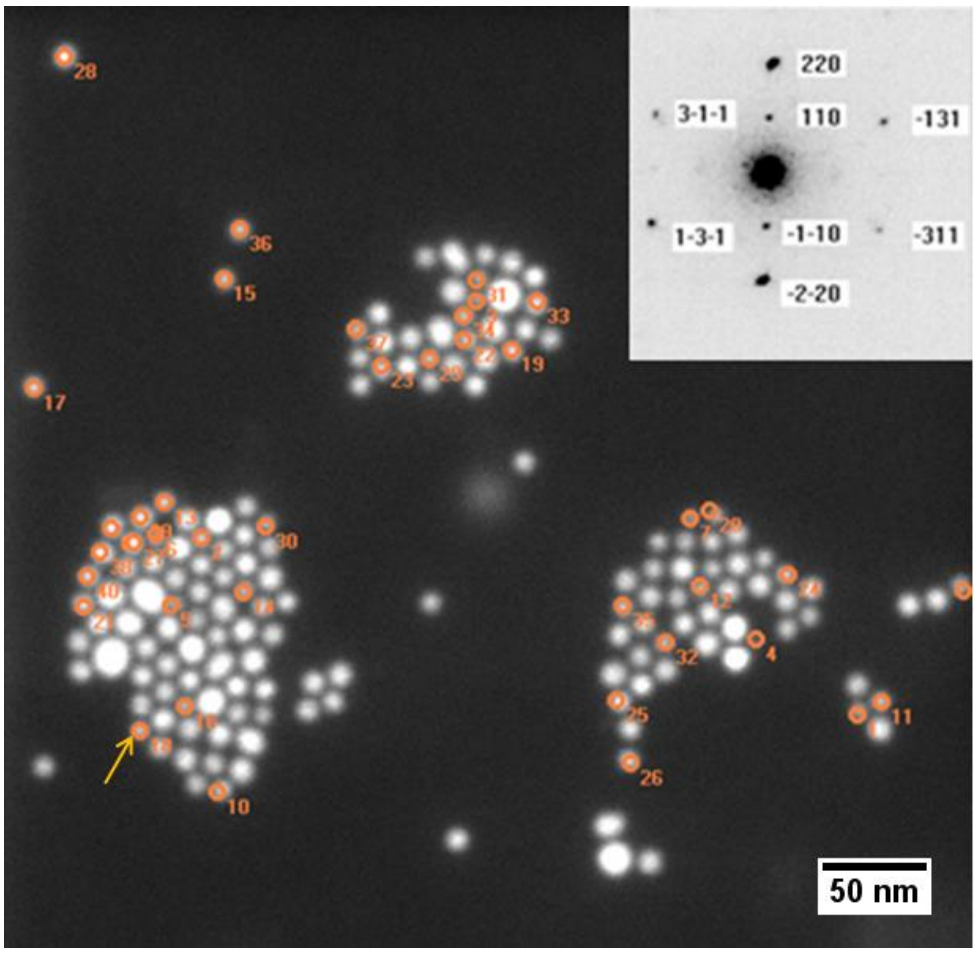

Figure 1.5: Parallel nanobeam diffraction pattern taken from a copper gold nanoparticle indicated by an arrow.

1.3.2.4 Electron Tomography

In conventional transmission electron microscopy, the image is taken from two-dimensional (2D) projection of a three-dimensional (3D) object; therefore, the spatial information in third dimension is hidden in 2D image. Without series of image analysis and simulation the 3D spatial information cannot be extracted. Electron tomography, one of 3D

electron microscopy technique, is developed to reconstruct 3D morphology of nanoparticles.[7, 8] A typical process of electron tomography requires 2D images taken from -75° to 75° of alpha tilting. Thereafter, the data series is reconstructed through reconstruction algorithm to restore 3D morphology of the 3D object. Figure 1.6 shows an example of tomography reconstruction of a gold nanowire with 5nm in thickness.

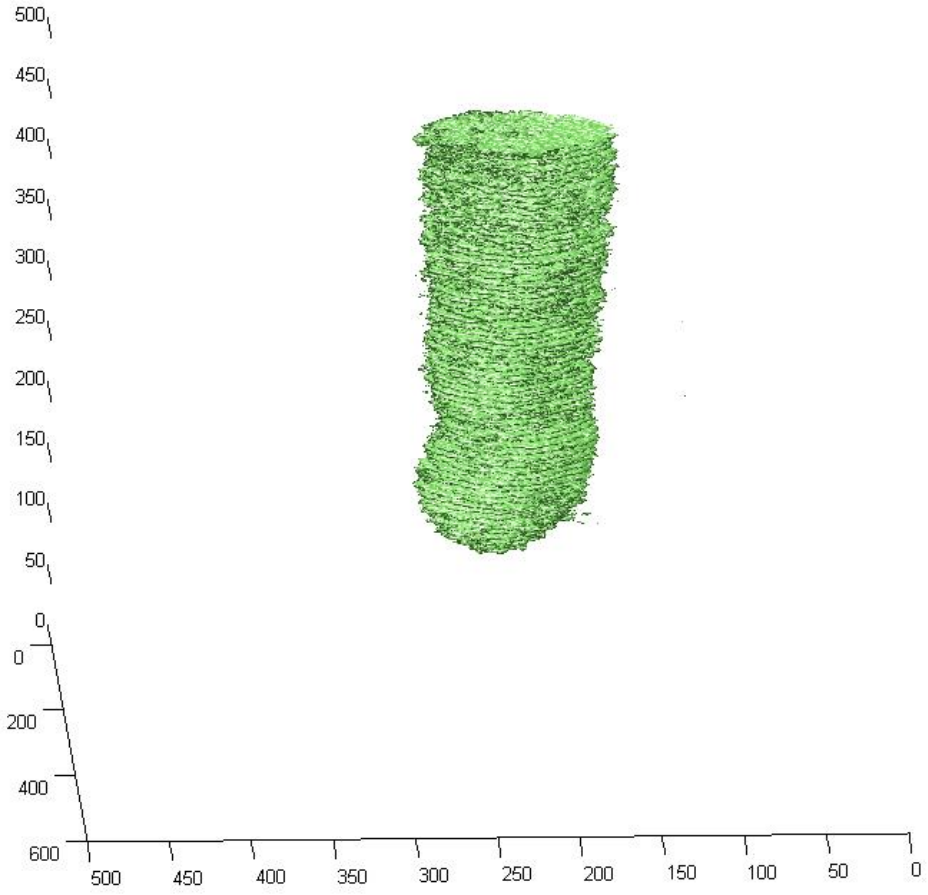

Figure 1.6: Electron tomography reconstruction of a gold nanowire.

1.4 Twinning in Nanowires

Twinning is a common strain-free defect often observed in metallic and semiconductor nanowires and bulks [6]; moreover, the presence of twinning can affect physical properties of the materials. Therefore it is my interest to study the relationship between structural defect(s)

and physical properties of the materials.

It has been reported that twinning can affect mechanical and optoelectronic properties of nanowires.[6, 11, 12, 16] For example, the band gap energy of semiconductor nanowires can be engineered by introducing twinning to the nanowires and the yield strength of metallic nanowires can be enhanced by having twining in the nanowires. Hence, twinning can serve as building block to tune physical properties of nanowires.

Although there are several proposed mechanisms for twinning formation [19, 26-29] based on possible chemical interaction in solution, the detailed mechanism of twinning formation in nanowires has not been clarified yet. Thus, I aimed to investigating the twining formation in nanowires and explain why having multiple twinning will facilitate the growth of fcc nanowires from surface/twin boundary energies and geometry balance standpoint. In this dissertation, a comprehensive studying of fabrication and characterization of nanowires is presented and a geometrical model[5] is developed to interpret the formation of twinning in nanowires.

1.5 Stacking Fault Energy and Formation of Twins

Slip and deformation twinning [30, 31] are two essential modes in plastic deformation in metals. In fcc metals, the tendency to form deformation twinning is often predicted by their stacking fault energy and this prediction is based on empirical observation of deformation twinning in fcc metals with low stacking fault energy. [32, 33]

In this dissertation, twin boundary energy was used among the main text rather than conventional stacking fault energy. Based on the first-principles calculations previously reported by Crampin et al., the ratio of twin boundary energy to stacking fault energy was estimated to be approximately one to two.[34]

1.6 Objectives

Individual chapter in this dissertation is dedicated to resolve a specific problem regarding nanowires fabrication, nanowires characterization and twinning formation in nanowires. The objective of the individual chapter is listed as follows.

1. First of all, it is reported that twinning can generally enhance mechanical properties of <111> oriented metallic nanowires; however, the formation mechanism of twinning in nanowires is still not fully understood. Therefore my objective in Chapter two is to investigate the influence of twin boundary energy and surface energy on twinning formation in nanowires. In this research, two materials were chosen as source materials to fabricate <111> oriented nanowires. One is gold which has low twin boundary energy and the other is platinum which has relative high twin boundary energy to gold. Once gold and platinum nanowires were fabricated, a detailed characterization was carried out to analyze the atomic structure of the nanowires. Furthermore, a linear geometric model was introduced to elucidate the formation of twinning in these nanowires.

2. Understanding three-dimensional distribution of fine twinning and other defected structure in metallic nanowires is essential in evaluating mechanical property of the nanowires. One powerful technique nowadays to acquire structural information of nanowires in 3D is electron tomography. The current resolution limit of electron tomography is at 2.4 angstrom [8]; however, with current resolution, individual atom in a defected structure cannot be fully located. Therefore, a technique that has higher resolution to resolve individual atom in nanowires is desired. My objective in Chapter three is to develop an new electron tomography technique to surpass the current resolution limit.

3. Diffraction pattern is a common technique in TEM to characterize crystal structure of nanowires. In conventional diffraction pattern analysis, the measurement of d-spacing is often accomplished manually. To promote the efficiency of diffraction analysis, a software tool for automatic diffraction analysis is desired. My objective in Chapter four is to develop a software tool to analyze diffraction patterns automatically and facilitate diffraction analysis.

4. To study twinning formation in <111> oriented nanowire, fabrication of nanowires is a must. The objective of Chapter five is to investigate the change of morphology in platinum nanowires by varying heat treatment time and temperature in solution-phase chemical synthesis. Eventually the synthesis condition can be optimized to fabricate <111> oriented platinum nanowires with high aspect ratio.

5. Barium titanate is a ferroelectric material. It has potential application in non-volatile memory device [35]; however, the ferroelectric property is crystallographic orientation dependent.[20] Therefore there is a need to control crystal growth of barium titanate thin film. Yuan Zhou is a PhD candidate in Virginia Tech and he has grown <111> oriented barium titanate columnar structures by PLD. The columnar structure has similar morphology to nanowires. Chapter six is a collaboration work between Mr. Yuan Zhou (MSE) and myself. My objective in Chapter six is to study the twining formation in barium titanate columnar structure and the growth orientation of the columnar structure.

References

[1] D. Alloyeau, C. Ricolleau, T. Oikawa, C. Langlois, Y. Le Bouar, A. Loiseau, STEM nanodiffraction technique for structural analysis of CoPt nanoparticles, Ultramicroscopy, 108 (2008) 656-662.

[2] J.M. Cowley, Electron nanodiffraction: Progress and prospects, Journal of Electron Microscopy, 45 (1996) 3-10.

[3] K.J. Ganesh, M. Kawasaki, J.P. Zhou, P.J. Ferreira, D-STEM: A Parallel Electron Diffraction Technique Applied to Nanomaterials, Microscopy and Microanalysis, 16 (2010) 614-621.

[4] H. He, C. Nelson, A method of combining STEM image with parallel beam diffraction and electron-optical conditions for diffractive imaging, Ultramicroscopy, 107 (2007) 340-344.

[5] J.E. Taylor, J.W. Cahn, C.A. Handwerker, GEOMETRIC .1. MODELS OF

CRYSTAL-GROWTH, Acta Metallurgica Et Materialia, 40 (1992) 1443-1474.
[6] E.L. Wood, F. Sansoz, Growth and properties of coherent twinning superlattice nanowires, Nanoscale, 4 (2012) 5268-5276.
[7] H.S. Kim, Y. Myung, Y.J. Cho, D.M. Jang, C.S. Jung, J. Park, J.-P. Ahn, Three-Dimensional Structure of Twinned and Zigzagged One-Dimensional Nanostructures Using Electron Tomography, Nano Lett., 10 (2010) 1682-1691.
[8] M.C. Scott, C.-C. Chen, M. Mecklenburg, C. Zhu, R. Xu, P. Ercius, U. Dahmen, B.C. Regan, J. Miao, Electron tomography at 2.4-angstrom resolution, Nature, 483 (2012) 444-U491.
[9] C.H. Wu, W.T. Reynolds, M. Murayama, A software tool for automatic analysis of selected area diffraction patterns within Digital Micrograph (TM), Ultramicroscopy, 112 (2012) 10-14.
[10] L. Cademartiri, G.A. Ozin, Ultrathin Nanowires - A Materials Chemistry Perspective, Advanced Materials, 21 (2009) 1013-1020.
[11] R.E. Algra, M.A. Verheijen, M.T. Borgstrom, L.-F. Feiner, G. Immink, W.J.P. van Enckevort, E. Vlieg, E.P.A.M. Bakkers, Twinning superlattices in indium phosphide nanowires, Nature, 456 (2008) 369-372.
[12] H. Feng, Y. Yang, Y. You, G. Li, J. Guo, T. Yu, Z. Shen, T. Wu, B. Xing, Simple and rapid synthesis of ultrathin gold nanowires, their self-assembly and application in surface-enhanced Raman scattering, Chemical Communications, (2009) 1984-1986.
[13] J.M. Bao, D.C. Bell, F. Capasso, J.B. Wagner, T. Martensson, J. Tragardh, L. Samuelson, Optical properties of rotationally twinned InP nanowire heterostructures, Nano Lett., 8 (2008) 836-841.
[14] B. Wei, K. Zheng, Y. Ji, Y. Zhang, Z. Zhang, X. Han, Size-Dependent Bandgap Modulation of ZnO Nanowires by Tensile Strain, Nano Letters, 12 (2012) 4595-4599.
[15] J.-E. Yang, C.-B. Jin, C.-J. Kim, M.-H. Jo, Band-gap modulation in single-crystalline Si1-xGex nanowires, Nano Letters, 6 (2006) 2679-2684.
[16] C. Deng, F. Sansoz, Near-Ideal Strength in Gold Nanowires Achieved through Microstructural Design, Acs Nano, 3 (2009) 3001-3008.

[17] Y. Xia, N. Trung Dac, M. Yang, B. Lee, A. Santos, P. Podsiadlo, Z. Tang, S.C. Glotzer, N.A. Kotov, Self-assembly of self-limiting monodisperse supraparticles from polydisperse nanoparticles, Nature Nanotechnology, 6 (2011) 580-587.
[18] Y. Huang, D.-H. Kim, Synthesis and Self-Assembly of Highly Monodispersed Quasispherical Gold Nanoparticles, Langmuir, 27 (2011) 13861-13867.
[19] C. Wang, S. Sun, Facile Synthesis of Ultrathin and Single-Crystalline Au Nanowires, Chemistry-an Asian Journal, 4 (2009) 1028-1034.
[20] D.Y. Kim, S.G. Lee, Y.K. Park, S.J. Park, EFFECT OF AMBIENT GAS-PRESSURE ON THE PREFERRED ORIENTATION OF BARIUM-TITANATE THIN-FILMS PREPARED BY PULSED-LASER DEPOSITION, Japanese Journal of Applied Physics Part 2-Letters, 34 (1995) 1564-1566.
[21] D.Y. Kim, S.G. Lee, Y.K. Park, S.J. Park, Tailoring of the preferred orientation and microstructure in the deposition of BaTiO3 thin films using pulsed laser deposition, Materials Letters, 40 (1999) 146-150.
[22] D.Y. Kim, S.G. Lee, Y.K. Park, S.J. Park, Variation of the preferred orientation with thickness in barium titanate thin films prepared by pulsed laser deposition, Japanese Journal of Applied Physics Part 1-Regular Papers Brief Communications & Review Papers, 36 (1997) 7307-7311.
[23] J.A. Thornton, HIGH-RATE THICK-FILM GROWTH, Annual Review of Materials Science, 7 (1977) 239-260.
[24] S. Rasappa, D. Borah, C.C. Faulkner, T. Lutz, M.T. Shaw, J.D. Holmes, M.A. Morris, Fabrication of a sub-10 nm silicon nanowire based ethanol sensor using block copolymer lithography, Nanotechnology, 24 (2013).
[25] Y.L. Zhu, S.J. Zheng, D. Chen, X.L. Ma, Microstructure tuning of epitaxial BaTiO3 (-) (x) thin films grown using laser molecular-beam epitaxy by varying the oxygen pressure, Thin Solid Films, 518 (2010) 3669-3673.
[26] M. Bernardi, S.N. Raja, S.K. Lim, Nanotwinned gold nanowires obtained by chemical synthesis, Nanotechnology, 21 (2010).
[27] A. Halder, N. Ravishankar, Ultrafine single-crystalline gold nanowire arrays by oriented

attachment, Advanced Materials, 19 (2007) 1854-+.
[28] Y. Lu, J.-p. Tu, C.-d. Gu, X.-h. Xia, X.-l. Wang, S.X. Mao, Growth of and methanol electro-oxidation by gold nanowires with high density stacking faults, Journal of Materials Chemistry, 21 (2011) 4843-4849.
[29] C. Wang, Y. Wei, H. Jiang, S. Sun, Bending Nanowire Growth in Solution by Mechanical Disturbance, Nano Lett., 10 (2010) 2121-2125.
[30] J.L. John Price Hirth, Theory of Dislocations, Krieger Pub Co, 1992.
[31] J.W. Christian, S. Mahajan, DEFORMATION TWINNING, Progress in Materials Science, 39 (1995) 1-157.
[32] N. Bernstein, E.B. Tadmor, Tight-binding calculations of stacking energies and twinnability in fcc metals, Physical Review B, 69 (2004).
[33] E.B. Tadmor, N. Bernstein, A first-principles measure for the twinnability of FCC metals, Journal of the Mechanics and Physics of Solids, 52 (2004) 2507-2519.
[34] S. Crampin, K. Hampel, D.D. Vvedensky, J.M. Maclaren, THE CALCULATION OF STACKING-FAULT ENERGIES IN CLOSE-PACKED METALS, Journal of Materials Research, 5 (1990) 2107-2119.
[35] W.S. Yun, J.J. Urban, Q. Gu, H. Park, Ferroelectric properties of individual barium titanate nanowires investigated by scanned probe Microscopy, Nano Letters, 2 (2002) 447-450.

Chapter 2

Twinning in <111>-Oriented Ultrathin Gold Nanowires: Structural Characterization and Energetics

2.1 Background

Achieving synthetic control of twinning in nanowires is of interest because it may offer a means of tuning the optoelectronic and physical properties of nanowires.[1-8] For example, it is reported that the band gap energy of wurtzite structure at a twin boundary is higher than the zinc blende structure in InP nanowires and the appearance of twinning can shift the optical absorption range of the nanowires.[9] Furthermore, molecular dynamics simulations predict the yield strength of gold nanowires can be enhanced by multiple twins.[1, 6]

One nanowire system in which twins have been observed is ultrathin gold nanowires (diameter < 10 nm) with a <111> crystallographic growth orientation produced via solution-phase chemical synthesis methods.[10-16] Several explanations have been proposed for why twins are present in gold nanowires. They are suggested to form as a result of oriented attachment-based growth[16], from mechanical disturbances during ultrasonication[17], from interactions with organic ligands[18], and from the emission of Shockley partial dislocations to relieve stress generated from stacking of the gold blocks[19]. All these mechanisms imply twins are a consequence of random, uncoordinated events.

An alternate possibility for why twins appear in nanowires is that they serve a structural role that facilitates nanowire growth. If so, nanotwins would be an intrinsic feature of nanowire growth. We postulate a simple geometrical model[20, 21] of twin formation in nanowires in which the incidence of twins is determined primarily by the balance between the surface and twin boundary energies[22-24] of the bulk material and the geometry (shape) of the nanowire. The model predicts the fastest growing nanowires of gold, which has a low twin boundary

energy, should contain twins, whereas the fastest growing nanowires of platinum, which has a high twin boundary energy, should be twin-free. In the work presented here, a detailed structural characterization of gold and platinum nanowires was employed to test this hypothesis, explore the role of twinning during the growth of metallic nanowires, and identify the factors responsible for multiple twinning. We also discuss our observations of twinning superlattices[5] in gold nanowires within the framework of the growth model.

2.2 Results and Discussion

The average size of synthesized gold nanowires was measured from TEM BF images. The gold nanowires had an average diameter of 6 nm (+/- 3 nm, calculated from 200 wires), and an average length of 303 nm (+/- 192nm, calculated from 100 wires). Energy Dispersive X-ray Spectroscopy (EDS) spectra and conventional selected area electron diffraction (SAED) patterns collected from multiple nanowires indicated the nanowires were pure gold with the face centered cubic (fcc) structure. The platinum nanowires had an average diameter of 10 nm (+/- 1 nm, calculated from 150 wires), and an average length of 48 nm (+/- 20 nm, calculated from 100 wires). EDS and conventional SAED patterns also indicated the nanowires were pure platinum with the fcc structure. The diameters and lengths of the nanowires were measured from recorded TEM images using Image J software[25].

HRTEM showed both gold nanowires and platinum nanowires had one of the {111} planes oriented perpendicular to the longitudinal axe of the wires; thus, both types of nanowires had grown along a <111> crystallographic direction. Other structural features were different between the two types of nanowires. The gold nanowires contained multiple twins whereas platinum nanowires were free from such defects. A typical HRTEM image of multiple twins in gold nanowires is shown in Figure 2.1(a), and a schema showing two {111} atomic layers between adjacent twin boundaries is drawn as an inset in Figure 2.1 (a). To confirm the presence of twins, the Fast Fourier transform (FFT) of the corresponding area in Figure 2.1(a) was examined. Instead of showing the regular spot pattern normally expected from a defect-free single crystal, we observed streaks of multiple reflection spots along the <111> direction, Figure 2.1(b). A simulated diffraction pattern, Figure 2.1(c), was calculated from the twinning

superlattice[5] structure shown in the inset of Figure 2.1(a). The match between the simulated pattern and the experimental FFT pattern confirms the twinned structure interpretation of the nanowire.

The platinum nanowires, on the other hand, displayed no twinning, as confirmed by multiple HRTEM images such as that in Figure 2.1(d). A unit cell of platinum single crystal is schematically shown in the inset. A FFT of the HRTEM image of the platinum nanowire is presented in Figure 2.1 (e), which shows the spot pattern expected from defect free single crystal fcc structure. A simulated diffraction pattern of a defect-free platinum single crystal (Figure 2.1(f)) matched our experimental FFT, confirming that no twins were present.

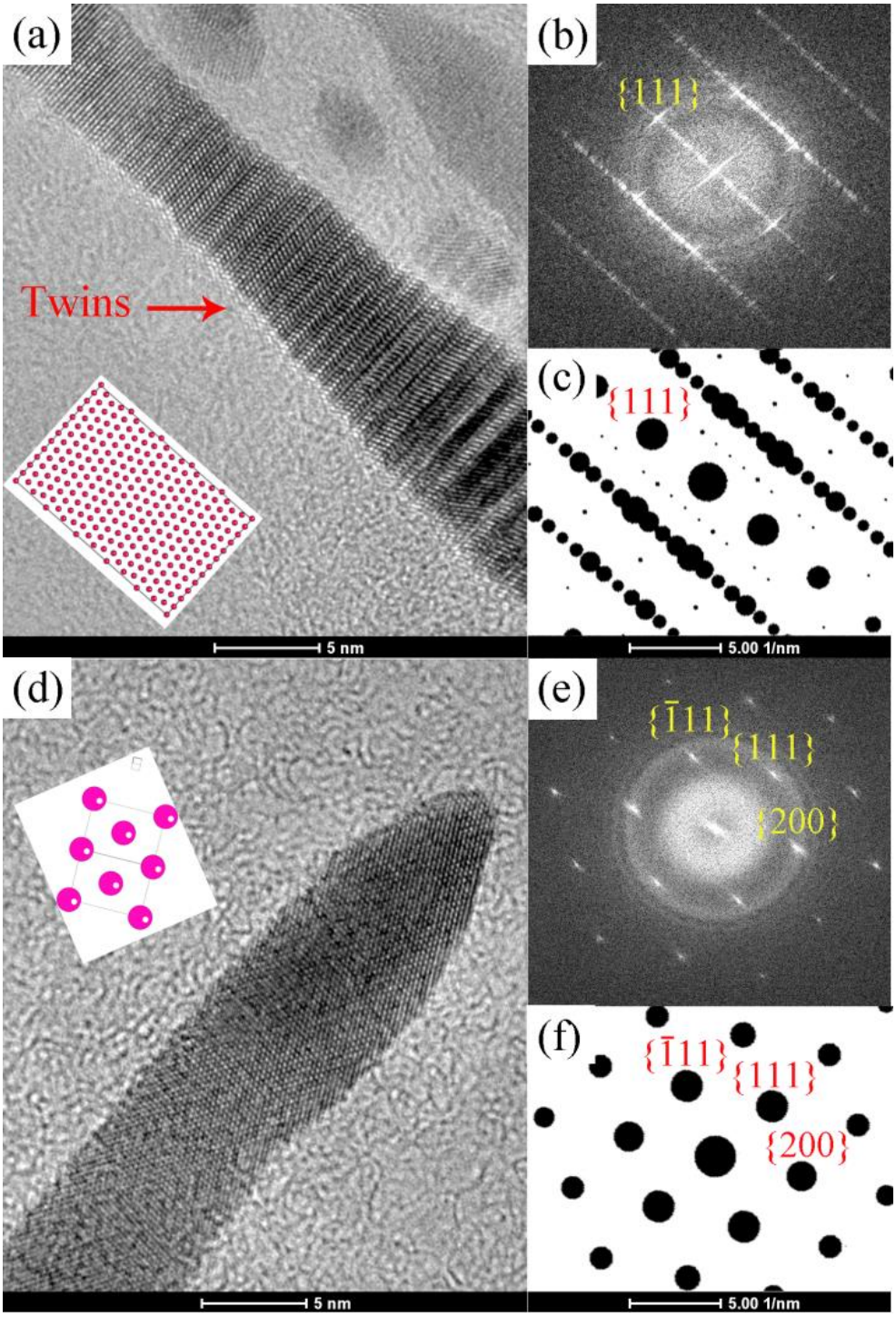

Figure 2.1: (a) HRTEM image of a gold nanowire with twins. A theoretical atomic structure of twinning superlattice with two {111} atomic layers ($2d_{111}$) between individual twin boundary is displayed as an inset. (b) Fast Fourier transform of (a). (c) Simulated diffraction pattern of twinning superlattice shown as inset in (a). (d) HRTEM image of a platinum nanowire with perfect single crystal structure. A platinum unit cell is drawn as an inset. (e) Fast Fourier transform of (d). (e) Simulated diffraction pattern of platinum unit cell shown as inset in (a).

Twin boundaries in gold nanowires are often arranged periodically as shown in Figure 2.2(a). This periodic formation of twin boundaries is often designated as a twinning superlattice.[5] The close packed {111} planes of the fcc structure have a stacking sequence (ABCABCA…). Unlike the fcc structure, a twinned fcc structure allows the stacking sequence to change from forward stacking (ABCABCA…) to backward (CBACBAC…) stacking or vice versa at every twin boundary. The twinning superlattice observed in the gold nanowires often exhibits the stacking sequence: ABCBABC… as shown in the schema in Figure 2.2(b).

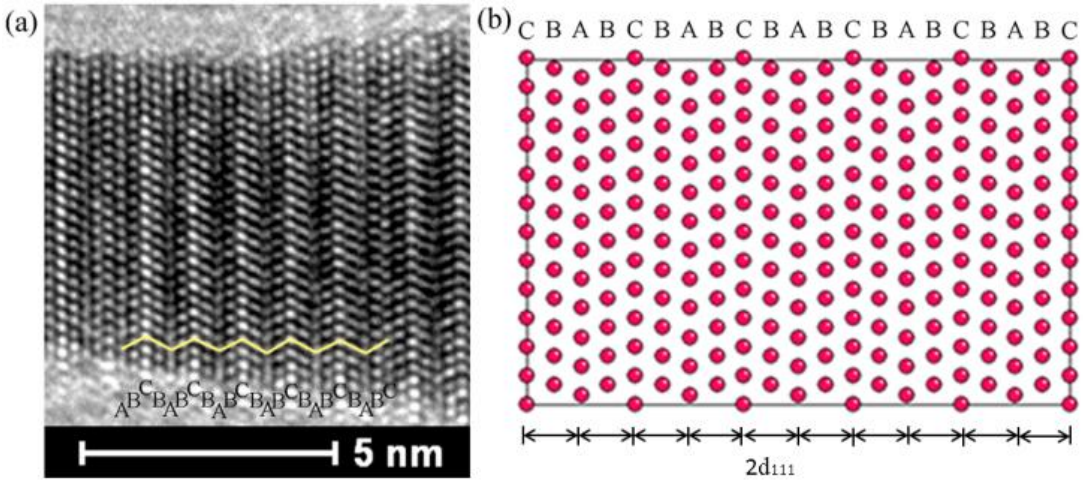

Figure 2.2: (a) HRTEM image of twinning superlattice with two {111} atomic layers ($2d_{111}$) between individual twin boundary. The stacking sequence of twinning superlattice has repeated unit of ABCB-. (2) A theoretical model of twinning superlattice with two {111} atomic layers ($2d_{111}$) between individual twin boundary.

As the area sampled by HRTEM imaging is highly limited, and twins could not be resolved in bright field TEM imaging (average distance between twin boundaries is 0.57 nm (+/- 0.38 nm), we utilized parallel nanobeam electron diffraction[26-30] to increase sampling and determine the prevalence of twinning. A total of 389 diffraction patterns were recorded along four different nanowires for a total length of 340 nm and analyzed by the SADP Tools.[31] Streaks of multiple reflection spots, which are a characteristic feature generated by multiple twinning, were observed in all the experimental diffraction patterns recorded. Five

representative diffraction patterns are presented in Figure 2.3 (a). We conclude from this data that twinning was a characteristic feature along the full lengths of the gold nanowires.

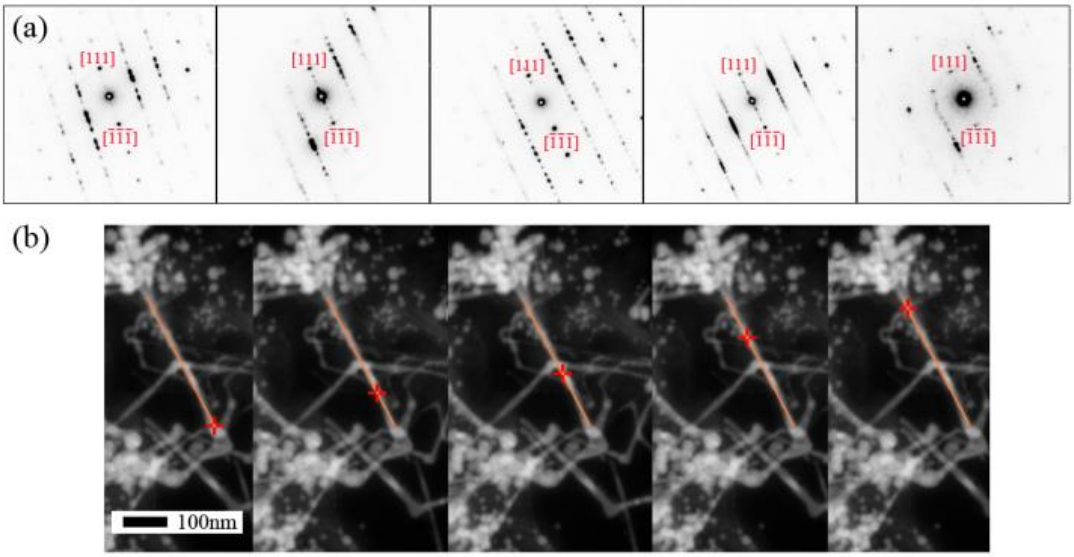

Figure 2.3: Parallel nanobeam diffraction analysis by STEM: (a) Diffraction patterns with inversed contrast taken from positions in a gold nanowire shown in (b).

To evaluate potential energetic considerations impacting the growth of the nanowires and formation of twins, we have postulated a classic geometric model[20, 21] for nanowire growth, in which the growth velocity of the nanowire surface is taken to be the product of a thermodynamic driving force and an effective mobility of the surface as shown in Equation (1) where V is the growth velocity of the wire, and P is the thermodynamic driving force for nanowire growth. The driving force is taken to be the free energy decrease during wire growth (i.e., the free energy decrease per unit volume change or pressure on the growing crystal front). The factor M is the mobility, which is defined as the ratio of V to P. Its magnitude depends upon the details of atomic attachment to the crystal and it is thus orientation dependent. The activation energy barriers for atomic attachment and any sequence of steps associated with the growth mechanism are effectively incorporated in the mobility of the growing surface. For the case of one-dimensional nanowire growth, the mobility of all crystal orientations except the one corresponding to the lengthening direction must necessarily be close to zero. In the two systems studied here, namely ultrathin gold and platinum nanowires, we have observed

growth only along the <111> orientation. It has been suggested in prior work that this strong preference for one growth direction is caused by chemical interactions between gold (or other metals constituting the nanowires) and surfactant molecules.[7, 12-14, 18] Thus, we limit the subsequent discussion to growth in only a <111> direction. Under this constraint and fixed synthesis conditions, we hypothesize the observed nanowire structure will correspond to the one with highest growth rate, and that will be the one that forms with the largest driving force, *P*.

$$V = MP \tag{1}$$

Figure 2.4(a) schematically shows a fcc crystal constrained to cylindrical shape with its longitudinal axis along a <111> orientation. The free energy change when a nanowire lengthens a small distance, δz, can be expressed by Equation (2) where γ is the side surface energy[22], γ_{twin} is the twin boundary energy between the lengthened volume and the original growth front plane of the wire[23], ν is the spatial frequency of twins (number of twins per unit length), *A* represents the area of the circular end of the wire, *C* is the circumference of the nanowire, and the quantity, $(C \cdot \delta z)$, represents the area of the curved cylindrical side surface. Rearranging Equation (2) gives δG/δz (Equation 3), the change in free energy as the wire grows and increment, δz, and this corresponds to the driving force, *P*, in Equation (1). Replacing the cylindrical side of the nanowire with polygonal sides consisting of low-energy facets can reduce the total surface energy of a nanowire as shown in Figure 2.4 (b), and Equation (4) is the driving force equation modified for nanowire faceting. The first term in Equation (4) that ($A\,\Delta G_f$), is negative where ΔG_f represents the free energy of formation (Au(aq) --> Au(s)) per unit volume of the precipitating metal[32]. The remaining two terms are positive ($\sum_i C_i\ \gamma_i + A\,\gamma_{twin}\ \nu$) [22, 23]and are associated with the energy required to form the new surfaces and internal twin boundaries (if twins are present). The smaller the magnitude of these positive terms, the greater the driving force available for growth.

$$\delta G_{lengthening} = (A \cdot \delta z)\,\Delta G_f + (C \cdot \delta z)\,\gamma + A\,\gamma_{twin}\,(\nu \cdot \delta z) \tag{2}$$

$$\frac{\delta G_{lengthening}}{\delta z} = P = A\,\Delta G_f + C\ \gamma + A\,\gamma_{twin}\nu \quad (3)$$

$$\frac{\delta G_{lengthening}}{\delta z} = P = A\,\Delta G_f + \sum_i C_i\ \gamma_i + A\,\gamma_{twin}\nu \quad (4)$$

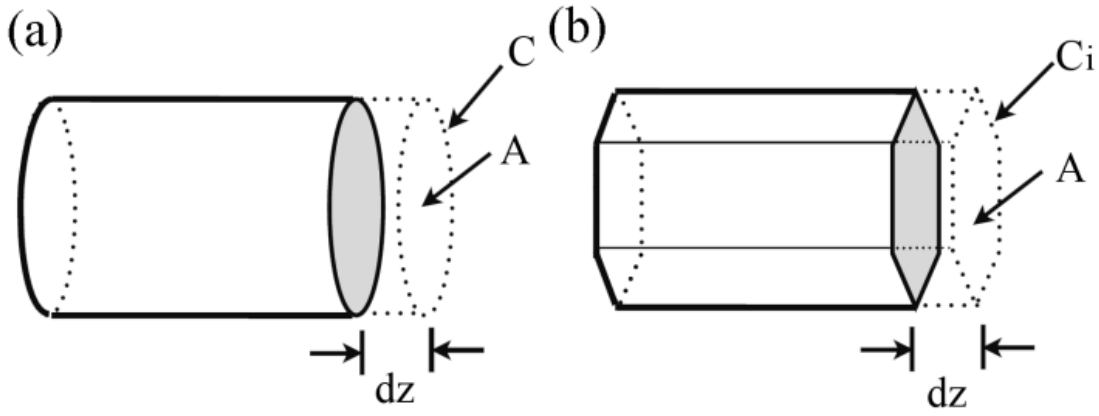

Figure 2.4: (a) A schematic fcc crystal constrained to a cylindrical shape with a long axis along a <111> direction. *A* represents the area of the circular end of the wire, *C* is the circumference of the wire, and the quantity, $C \cdot dz$, represents the area of the curved cylindrical surface. (b) By replacing the cylindrical surface in (a) with low-energy side surfaces the total surface energy of a nanowire can be reduced and *Ci* represents the length of the side of polygonal growth front.

Given the diameters of the nanowires studied (≤ 10 nm), the surface area to volume ratio is high, and thus surface energies are expected to significantly impact the energetics of nanowire growth. For metallic materials with the fcc crystal structure, the lowest surface energies are associated with the {111}, {100} and {110} planes. The relative magnitude of surface energies of these planes are in the following sequence: $\gamma_{111} < \gamma_{100} < \gamma_{110}$.[33] To maximize the driving force, low-energy side facets are favored as well as a defect-free crystal structure. However, when nanowires are constrained to grow in a <111> direction, the geometry of fcc lattice precludes the side facets from being enclosed entirely by {111} surfaces because the nanowire growth front shrinks and truncates the wire with a tetrahedral tip as shown in Figure 2.5(a). [34, 35] Two other energy-lowering options remain. One entails maintaining a perfect crystal structure but introducing higher-energy crystal surfaces, namely both {111} and {100} as

shown in Figure 2.5 (b). The other is to have all {111} surfaces, but introduce twins as shown in Figure 2.5 (c). Applying Equation (4) to these two cases yields Equations (5) and (6). When the driving forces for growth of the two types of structures are equal, the neither structure has a kinetic growth advantage. This condition corresponds to equating Equations (5) and (6), which leads to equation (7). Next, by deriving material dependent factors to the left side of the equation (7) and geometrical dependent factors to the right side of the equation (7), we have equation (8). In equation (8), all material dependent factors are collected in the factor, φ, and the factor, S includes all the shape-dependent factors. If $\varphi > S$ a nanowire is expected to grow with twins and if $\varphi < S$ a nanowire should grow without twins.

$$\frac{\delta G_{lengthening}}{\delta z} = A\,\Delta G_f + \sum_{i=1}^{x} C_i\ (\gamma_{111}) + \sum_{j=x}^{n} C_j\ (\gamma_{100}) \quad \text{(Without Twinning)} \qquad (5)$$

$$\frac{\delta G_{lengthening}}{\delta z} = A\,\Delta G_f + \sum_{i=1}^{n} C_i\ (\gamma_{111}) + A\,\gamma_{twin}\,\nu \qquad \text{(Twinning)} \qquad (6)$$

$$A\,\gamma_{twin} = \sum_{j=x}^{n} C_j\ (\gamma_{100} - \gamma_{111}) \qquad (7)$$

$$\frac{(\gamma_{100}-\gamma_{111})}{\gamma_{twin}} = \frac{A\nu}{\sum_{j=x}^{n} C_j}\ , \left(\frac{(\gamma_{100}-\gamma_{111})}{\gamma_{twin}} = \varphi, \quad \frac{A\nu}{\sum_{j=x}^{n} C_j} = S\right) \qquad (8)$$

The material dependent factor φ can be evaluated from the bulk surface energies and twin boundary energies of gold and platinum.[22, 23] Since the twin boundary energy of gold is an order lower than the twin boundary energy of platinum, the factor φ of gold is an order higher than the factor φ of platinum. This makes it easier for gold nanowire to form twinning during nanowire growth. For factor S, we can estimate it from the geometries of the nanowires. To simply estimate the geometrical factors, nanowires are assumed to have cylindrical shape. The factor A represents the cross-section area of the nanowire. For circular gold nanowires with average diameter of 6nm and circular platinum nanowires with average diameter of 10nm, the A factor is 28 nm^2 and 79 nm^2, respectively. The factor ν is the number of twins per unit length and it can be taken as the reciprocal of the average spacing between twin boundaries in a nanowire containing twins. The minimum spacing between twin boundaries that an fcc nanowire can have is two {111} atomic planes (or $2d_{111}$) as shown in Figure 5(d). Using the maximum ν factor ($1/2d_{111}$) to estimate the upper bound of S, the ν factors for gold and

platinum wires are 2.08 and 2.27 (1/nm), respectively. Finally, the factor $\sum_{j=x}^{n} C_j$ represents the proportion of the {100} side surfaces to the total side surface multiplied by the circumference of a nanowire per unit length, δz. Figure 2.5 (e) shows a single crystal nanowire with lengthened value of $2d_{111}$ and there is one {100} side surface among two total side surfaces. Therefore factors $\sum_{j=x}^{n} C_j$ of gold and platinum nanowires can be estimated as one half of the circumference of 6nm circular nanowire and 10nm circular which are 9 nm and 16nm. Based on these estimated values, the shape dependent factor, S, for gold and platinum can be evaluated.

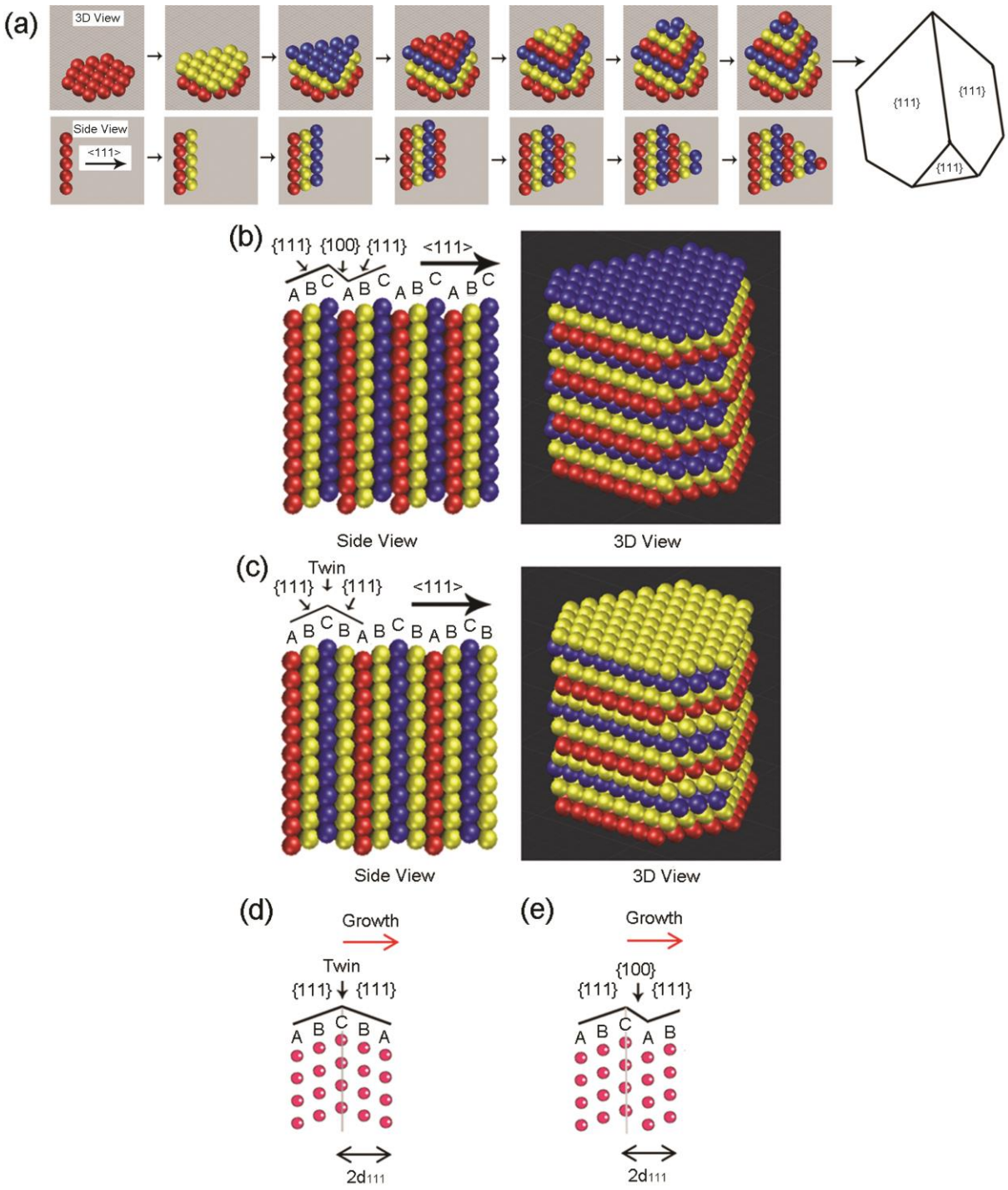

Figure 2.5: (a) Schematic diagram of a nanowire growing in a <111> orientation with perfect single crystal structure and {111} side surfaces. During the growth, the nanowire growth front would shrink, resulting in truncation at a tetrahedral tip. (b) A nanowire with perfect single crystal structure grows in a <111> orientation with both {111} and {100} side surfaces. (c) By introducing multiple twin boundaries, a nanowire can grow in a <111> orientation with only {111} side surfaces. (d) The minimum spacing between twin boundaries that a fcc nanowire

can have is two d-spacing of {111} atomic planes ($2d_{111}$). (e) A single crystal nanowire with lengthened value of $2d_{111}$ has one {100} side surface among two total side surfaces.

Both φ and S for gold and platinum nanowires are listed in Table 1. Based upon the relative values of these coefficients, we predict that for gold and platinum nanowires produced with the same surfactant, gold nanowires should grow with twins and be enclosed entirely by {111} facets, while platinum nanowires should grow defect-free crystal structures and be enclosed by a combination of {111} and {100} facets. Our data agrees with these predictions.

Table 2.1: Twin boundary energies, surface free energies, coefficients φ and S for gold and platinum.

	γ_{twin} (mJ/m^2)	γ_{111} (mJ/m^2)	γ_{100} (mJ/m^2)	φ	S
Gold	15	1283	1627	23	6 (nanowire, Ø6nm)
Platinum	161	2299	2734	3	11(nanowire, Ø10nm)

*Twinned nanowires are expected when $\varphi > S$.

A twinning superlattice with $2d_{111}$ between periodic twin boundaries was frequently observed in gold nanowires as shown in Figure 2.2 (a) and the presence of the periodically-existed twin boundaries can be explained from the following energetic standpoint. From previous discussion, we know that to maximize the driving force P it is energetically favorable to have twins in gold nanowires. From our experimental observation and several proposed mechanism regarding surfactant assisted nanowire growth [7, 12-14, 18], we also know that the nanowires have preferred growth orientation in a <111> direction. Therefore, Figure 2.6 shows that to prevent gold nanowires from growing into <$\bar{1}\bar{1}$2> direction a nanowire should have twins as frequently as possible to maintain the growth direction in a <111> direction. Meanwhile, we also know that the minimum spacing between twin boundaries that a fcc crystal can have is $2d_{111}$. Thus, it is energetically favorable to have twinned gold nanowires with spacing of $2d_{111}$ between adjacent twin boundaries. Besides the observation of the spacing

between twin boundaries as $2d_{111}$ in twinning superlattice, the average spacing between twin boundaries in our gold nanowire is $2.4d_{111}$ which is close to the expected spacing of the expect structure.

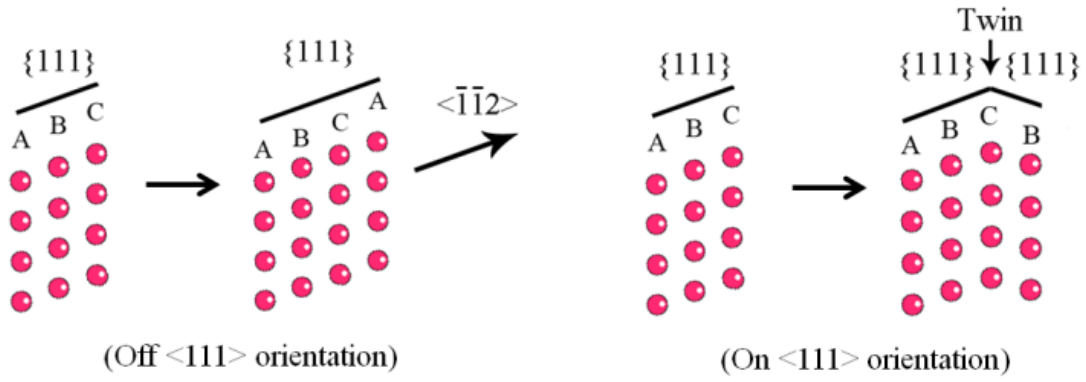

Figure 2.6: Twinning can lead nanowire growth to stay on the a <111> preferred orientation.

2.3 Summary

We present a detailed structural characterization of gold and platinum nanowires via high-resolution transmission electron microscopy (HRTEM) and parallel nanobeam electron diffraction. Results show multiple twinning is a general structural feature in gold nanowires, and the twin spacing is sufficiently regular to produce a twinning superlattice. Although structurally identical to gold, platinum nanowires grow as twin-free single crystals. A growth model is developed to account for the observed structural difference between gold and platinum nanowires. The model considers the effects of surface energy and defect energy on the free energy change driving nanowire growth. Under the maximum growth rate hypothesis, a balance between the shape of the nanowire and the relative magnitudes of the surface and twin boundary energies explains the presence of regular twins in gold and the absence of twins in platinum nanowires.

2.4 Methods

2.4.1 Preparation of Gold Nanowires

Gold nanowires were prepared via a solution-phase chemical synthesis derived from prior work as follows.[12] Gold chloride (30 wt%, Sigma-Aldrich) was used as a precursor and oleylamine (70%, Sigma-Aldrich) served as surfactant, reducing agent, and solvent. A mass of 0.06 mmol of gold chloride was mixed with 20 mL of oleylamine in a 50 mL vial under air at room temperature (21-25 ℃) then ultrasonicated (85 watts) for 15 min. The precursor and solvent were fully mixed at the end of sonication and the solution presented a reddish-orange color. After aging at room temperature for a day without mechanical disturbance (no stirring or sonication), a white gel-like precipitate formed in the bottom of the vial, and the color of the solution changed from reddish-orange to light yellow. After aging at room temperature for fifty days, the color of the white gel-like precipitate changed to dark purple. Ethanol was added to the reaction solution (3:1 ratio) to remove the surfactant on the precipitates and the mixture was then centrifuged to isolate the dark purple precipitate, which was then dispersed in hexane. Transmission electron microscopy (TEM) samples were prepared by dropping the hexane suspension onto carbon-coated copper grids (Cu-200HD, Pacific Grid-Tech) and allowing them to air-dry. The grids were subsequently washed with ethanol to remove excess surfactant.

2.4.2 Preparation of Platinum Nanowires

To prepare platinum nanowires, we followed a chemical synthesis route similar to that of the gold nanowires.[12, 36] A mass of 0.4 mmol of chloroplatinic acid (as an 8 wt% solution in H_2O, Sigma-Aldrich) was mixed with 40 mL of oleylamine in a 100 mL round-bottom three-necked flask. The three-necked flask was connected to a Schlenk line and the solution was flushed with argon for 15 minutes under magnetic stirring. Under continued argon flow and stirring, the solution was heated to 60 ℃ for 20 minutes to mix the yellow reaction solution. The magnetic stirrer was turned off to reduce the possibility of mechanical turbulence inducing twinning in the nanowires.[17] The mixed solution then was heated to 210 ℃ at a rate of 3 ℃ per minute and maintained at this temperature for 45 minutes after which it was allowed to cool naturally to room temperature. The final solution presented a black color. Ethanol was added to the reaction solution (3:1 ratio) to remove the surfactant. The mixture was then centrifuged to

isolate the black precipitate, which was subsequently dispersed in hexane. TEM samples of platinum nanowires were prepared by dropping the hexane suspension onto carbon-coated copper grids. Once the hexane suspension was dry, ethanol was used to wash the TEM grid to remove excess surfactant.

2.4.3 TEM Analysis

A FEI Titan 80-300 scanning/transmission electron microscope (S/TEM) was utilized for bright field (BF) imaging, high resolution transmission electron microscopy (HRTEM) and energy dispersive x-ray spectroscopy (EDS) analysis. The TEM was operated at 300 kV. A typical condition used for HRTEM imaging was a 70 um C2 aperture with an objective lens defocus of -58 nm. Parallel nanobeam electron diffraction was also performed in STEM mode with a 10 m C2 aperture and 480 mm camera length. The electron probe size for this parallel nanobeam electron diffraction was approximately 3 nm. The parallel nanobeam electron diffraction technique is a type of selected area electron diffraction technique that uses a nanometer sized, nearly parallel electron beam (convergence angle less than 0.12 mrad) to record electron diffraction patterns from the illuminated area.

References

[1] K.A. Afanasyev, F. Sansoz, Strengthening in gold nanopillars with nanoscale twins, Nano Lett., 7 (2007) 2056-2062.

[2] E.L. Wood, F. Sansoz, Growth and properties of coherent twinning superlattice nanowires, Nanoscale, 4 (2012) 5268-5276.

[3] Z. Ikonic, G.P. Srivastava, J.C. Inkson, ELECTRONIC-PROPERTIES OF TWIN BOUNDARIES AND TWINNING SUPERLATTICES IN DIAMOND-TYPE AND ZINCBLENDE-TYPE SEMICONDUCTORS, Physical Review B, 48 (1993) 17181-17193.

[4] Z. Ikonic, G.P. Srivastava, J.C. Inkson, OPTICAL-PROPERTIES OF TWINNING SUPERLATTICES IN DIAMOND-TYPE AND ZINCBLENDE-TYPE SEMICONDUCTORS, Physical Review B, 52 (1995) 14078-14085.

[5] R.E. Algra, M.A. Verheijen, M.T. Borgstrom, L.-F. Feiner, G. Immink, W.J.P. van

Enckevort, E. Vlieg, E.P.A.M. Bakkers, Twinning superlattices in indium phosphide nanowires, Nature, 456 (2008) 369-372.

[6] C. Deng, F. Sansoz, Near-Ideal Strength in Gold Nanowires Achieved through Microstructural Design, Acs Nano, 3 (2009) 3001-3008.

[7] C. Wang, S. Sun, Facile Synthesis of Ultrathin and Single-Crystalline Au Nanowires, Chemistry-an Asian Journal, 4 (2009) 1028-1034.

[8] H. Kura, T. Ogawa, Synthesis and growth mechanism of long ultrafine gold nanowires with uniform diameter, Journal of Applied Physics, 107 (2010).

[9] J.M. Bao, D.C. Bell, F. Capasso, J.B. Wagner, T. Martensson, J. Tragardh, L. Samuelson, Optical properties of rotationally twinned InP nanowire heterostructures, Nano Lett., 8 (2008) 836-841.

[10] L. Cademartiri, G.A. Ozin, Ultrathin Nanowires - A Materials Chemistry Perspective, Advanced Materials, 21 (2009) 1013-1020.

[11] H. Feng, Y. Yang, Y. You, G. Li, J. Guo, T. Yu, Z. Shen, T. Wu, B. Xing, Simple and rapid synthesis of ultrathin gold nanowires, their self-assembly and application in surface-enhanced Raman scattering, Chemical Communications, (2009) 1984-1986.

[12] Z. Huo, C.-k. Tsung, W. Huang, X. Zhang, P. Yang, Sub-two nanometer single crystal Au nanowires, Nano Letters, 8 (2008) 2041-2044.

[13] X. Lu, M.S. Yavuz, H.-Y. Tuan, B.A. Korgel, Y. Xia, Ultrathin gold nanowires can be obtained by reducing polymeric strands of oleylamine-AuCl complexes formed via aurophilic interaction, Journal of the American Chemical Society, 130 (2008) 8900-+.

[14] N. Pazos-Perez, D. Baranov, S. Irsen, M. Hilgendorff, L.M. Liz-Marzan, M. Giersig, Synthesis of flexible, ultrathin gold nanowires in organic media, Langmuir, 24 (2008) 9855-9860.

[15] C. Wang, Y. Hu, C.M. Lieber, S. Sun, Ultrathin Au nanowires and their transport properties, Journal of the American Chemical Society, 130 (2008) 8902-+.

[16] A. Halder, N. Ravishankar, Ultrafine single-crystalline gold nanowire arrays by oriented attachment, Advanced Materials, 19 (2007) 1854-+.

[17] C. Wang, Y. Wei, H. Jiang, S. Sun, Bending Nanowire Growth in Solution by Mechanical

Disturbance, Nano Lett., 10 (2010) 2121-2125.

[18] M. Bernardi, S.N. Raja, S.K. Lim, Nanotwinned gold nanowires obtained by chemical synthesis, Nanotechnology, 21 (2010).

[19] Y. Lu, J.-p. Tu, C.-d. Gu, X.-h. Xia, X.-l. Wang, S.X. Mao, Growth of and methanol electro-oxidation by gold nanowires with high density stacking faults, Journal of Materials Chemistry, 21 (2011) 4843-4849.

[20] J.E. Taylor, J.W. Cahn, C.A. Handwerker, GEOMETRIC .1. MODELS OF CRYSTAL-GROWTH, Acta Metallurgica Et Materialia, 40 (1992) 1443-1474.

[21] A.E. Lobkovsky, A. Karma, M.I. Mendelev, M. Haataja, D.J. Srojovitz, Grain shape, grain boundary mobility and the Herring relation, Acta Materialia, 52 (2004) 285-292.

[22] L. Vitos, A.V. Ruban, H.L. Skriver, J. Kollar, The surface energy of metals, Surface Science, 411 (1998) 186-202.

[23] N. Bernstein, E.B. Tadmor, Tight-binding calculations of stacking energies and twinnability in fcc metals, Physical Review B, 69 (2004).

[24] E.B. Tadmor, N. Bernstein, A first-principles measure for the twinnability of FCC metals, Journal of the Mechanics and Physics of Solids, 52 (2004) 2507-2519.

[25] C.A. Schneider, W.S. Rasband, K.W. Eliceiri, NIH Image to ImageJ: 25 years of image analysis, Nature Methods, 9 (2012) 671-675.

[26] J.M. Cowley, Electron nanodiffraction: Progress and prospects, Journal of Electron Microscopy, 45 (1996) 3-10.

[27] J.M. Cowley, Applications of electron nanodiffraction, Micron, 35 (2004) 345-360.

[28] K.J. Ganesh, M. Kawasaki, J.P. Zhou, P.J. Ferreira, D-STEM: A Parallel Electron Diffraction Technique Applied to Nanomaterials, Microscopy and Microanalysis, 16 (2010) 614-621.

[29] D. Alloyeau, C. Ricolleau, T. Oikawa, C. Langlois, Y. Le Bouar, A. Loiseau, STEM nanodiffraction technique for structural analysis of CoPt nanoparticles, Ultramicroscopy, 108 (2008) 656-662.

[30] H. He, C. Nelson, A method of combining STEM image with parallel beam diffraction and electron-optical conditions for diffractive imaging, Ultramicroscopy, 107 (2007) 340-344.

[31] C.H. Wu, W.T. Reynolds, M. Murayama, A software tool for automatic analysis of selected area diffraction patterns within Digital Micrograph (TM), Ultramicroscopy, 112 (2012) 10-14.

[32] J. Dolfing, D.B. Janssen, Estimates of Gibbs free energies of formation of chlorinated aliphatic compounds, Biodegradation, 5 (1994) 21-28.

[33] J. Luis Elechiguerra, J. Reyes-Gasga, M. Jose Yacaman, The role of twinning in shape evolution of anisotropic noble metal nanostructures, Journal of Materials Chemistry, 16 (2006) 3906-3919.

[34] H.W. Shim, Y. Zhang, H. Huang, Twin formation during SiC nanowire synthesis, Journal of Applied Physics, 104 (2008).

[35] F. Sansoz, H. Huang, D.H. Warner, An atomistic perspective on twinning phenomena in nano-enhanced fcc metals, Jom, 60 (2008) 79-84.

[36] L.-M. Lacroix, C. Gatel, R. Arenal, C. Garcia, S. Lachaize, T. Blon, B. Warot-Fonrose, E. Snoeck, B. Chaudret, G. Viau, Tuning Complex Shapes in Platinum Nanoparticles: From Cubic Dendrites to Fivefold Stars, Angewandte Chemie-International Edition, 51 (2012) 4690-4694.

Chapter 3

Three-Dimensional Atomic Imaging through Stereo Vision

3.1 Background

Some of the unique physical attributes of nano-structured materials arise from three dimensional (3D) spatial features. One approach for revealing 3D features of crystalline nanoparticles involves creating a tomographic reconstruction from transmission electron micrographs. Electron tomographic reconstructions use algorithms to infer 3D geometry from a series of conventional 2D projections taken from different perspectives. However, it is difficult to achieve 3D atomic resolution with electron tomography because the 2D micrographs must be aligned with a spatial accuracy better than the imaged interatomic spacing. Discrete tomography of a perfect, periodic crystal is a promising strategy for achieving atomic resolution, but it relies upon an assumed structure model for the crystal, and since there is no universal theory capable of predicting atomic arrangements in metastable or defective crystals, it remains unclear if discrete tomography can be applied to materials containing non-periodic features. Here we demonstrate a model-free electron tomography technique for 3D imaging non-periodic structures containing defects. The technique employs intrinsic crystal features instead of extrinsic fiducial markers to achieve the alignment accuracy needed to reconstruct a crystal with atomic resolution. We apply it to determine the 3D geometry and atomic arrangements of a highly defective gold nanowire. Unlike traditional tomography approaches, the lattice positions within the crystal are located independently of the surface reconstruction using only two projection orientations. The method is applicable to a variety of materials and sample geometries, and it is capable of resolving defect structures such as nanoscale twins and dislocations. Because it produces an accurate 3D representation of the crystal lattice, it also enables highly accurate internal spatial measurements.

Several electron tomography strategies have been developed to achieve reconstructions

with full atomic-scale resolution. Jinschek et al. [1] employed phase contrast images and exit wave reconstructions to determine the shape of a small gold particle and the location of atoms within atomic columns via discrete tomography. Saghi et al. [2] proposed a hybrid technique utilizing phase contrast images to locate atom positions and particle silhouettes to reconstruct shape. Discrete tomography has also been developed using annular dark field scanning transmission electron microscopy (STEM) with statistical parameter estimation [3]. Van Dyck and Chen [4] demonstrated an alternate exit wave reconstruction using phase information of electrons scattered from atoms behaving as point sources.

There are practical challenges to implementing these strategies, however, including difficulty tilting a sample through large angles with enough mechanical precision to permit atomic resolution reconstruction, and the need to rely on an assumed structure model to infer atom positions along the electron beam direction. A model-free strategy was recently demonstrated [5], but accurate image alignment remains a barrier to reconstructing arbitrary nanostructured crystals with atomic resolution. To circumvent these difficulties, we have developed a model-free protocol that employs crystallography to enhance the precision of image acquisition and achieves atomic-scale 3D reconstruction in nanocrystalline samples tens of nanometers in size.

3.2 Results and Discussion

The approach separates extracting atomic arrangements and locating the sample surface from tilt series images into two separate tasks. The entire tilt series is taken using the normal to an important crystal plane as the rotation axis to ensure the tilt series has an angular precision substantially better than the mechanical precision typically achievable with a TEM sample stage. The lateral position of the images in the tilt series are aligned manually with reference to one or more intrinsic crystal features that can be located with spatial accuracy within the spacing of an atomic plane.

A tomographic reconstruction of a chemically synthesized gold nanowire approximately 5 nm in diameter and 22 nm in length was performed to demonstrate the method. The complete reconstruction includes 24,209 atoms.

A tilt series was taken in high-resolution (HR)-TEM mode with a spherical aberration coefficient of nearly zero. This particular type of nanowire grows along a [111] face-centered cubic crystal direction, so each wire is a long, narrow stack of close-packed (111) planes and the long axis of the wire is a perpendicular to the stack of planes. The (111) planes were used as the internal reference features to facilitate rotational tilting with high axial precision. The stacking of these planes does not adhere closely to the perfect …ABCABC… face-centered cubic stacking, and many of the (111) planes constitute twin boundaries and stacking faults perpendicular to the axis of the wire. The twin boundaries were used as the intrinsic crystal features to manually align the images of the tilt series with high lateral accuracy.

A series of images was recorded by tilting the nanowire through a ±60° angular range at approximately 5° intervals (Figure 3.1). After each tilt increment, the sample's tilt orientation was adjusted by taking a HRTEM image and inspecting its corresponding Fast Fourier Transform pattern to ensure the (111) planes perpendicular to the wire axis remained oriented parallel to the electron beam.

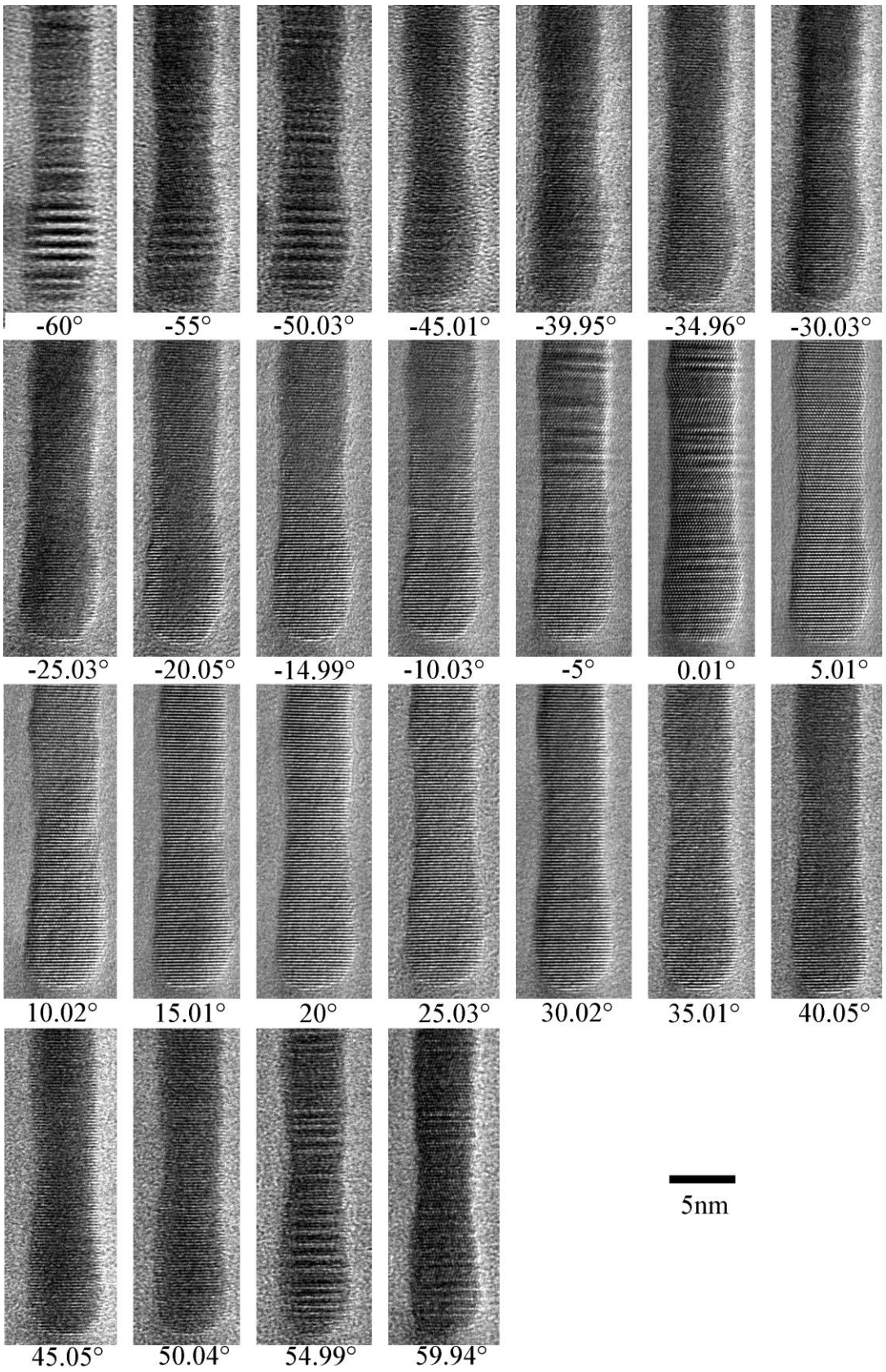

Figure 3.1: Two-dimensional tilt series images used to generate the 3D reconstruction. Horizontal scale marker represents 5 nm length.

In addition to ensuring a precise rotation axis, superimposing (111) lattice fringes in the tilt series images was used to establish correct alignment along the length of the nanowire. Manually aligning the twin boundaries in the tilt series effectively anchored all the (111) fringes to the correct (111) crystal planes. The red schematic planes in Figure 3.2 (a) represent twin boundaries suitable for aligning tilt-series images, and actual twin boundaries are evident in the tilt-series images of Figures 3.3. Any intrinsic crystal feature linked to specific atomic planes can be used for this purpose, but the easily identified twin boundaries that appeared in all the images of the tilt series were most convenient for the gold nanowire.

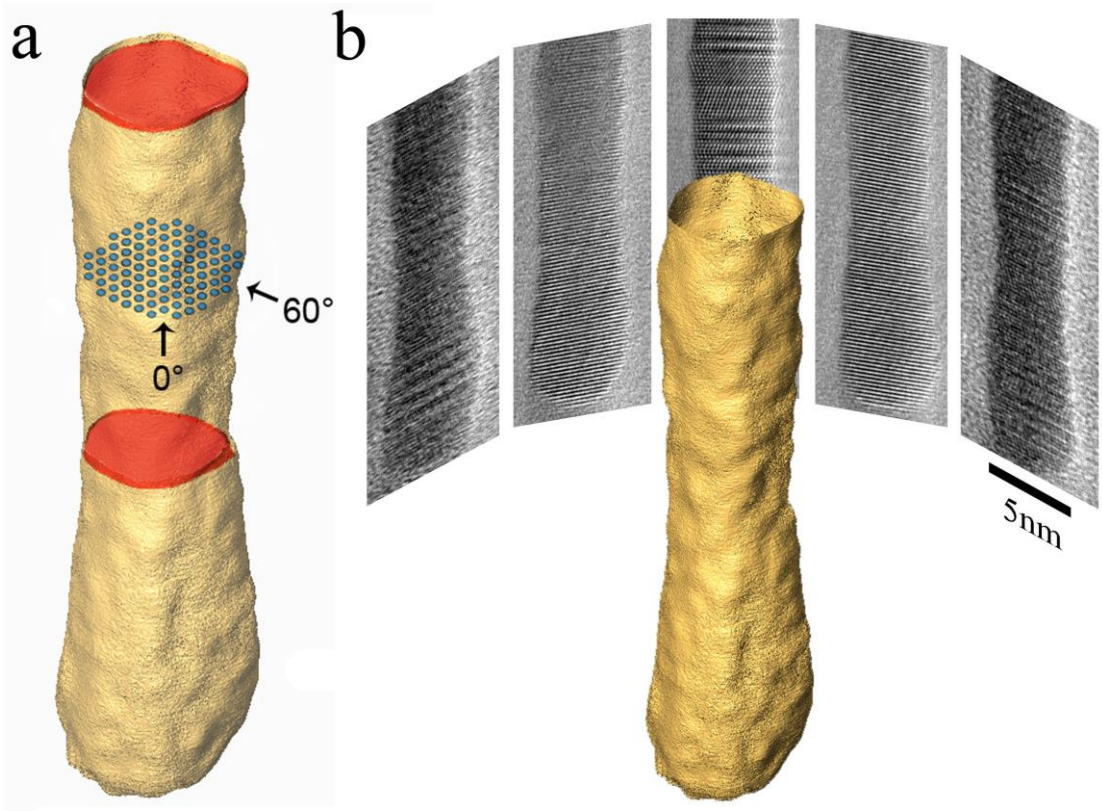

Figure 3.2: Schematic relationship between the reconstruction and TEM data (a) schematic showing two twin planes (red) suitable for aligning tilt-series images, and the atomic columns in one (111) plane viewed from the two directions of the epipolar projections; (**b**) relative position of projected tilt-series images and the tomographic reconstruction of the nanowire surface. Horizontal scale markers represent 5 nm length.

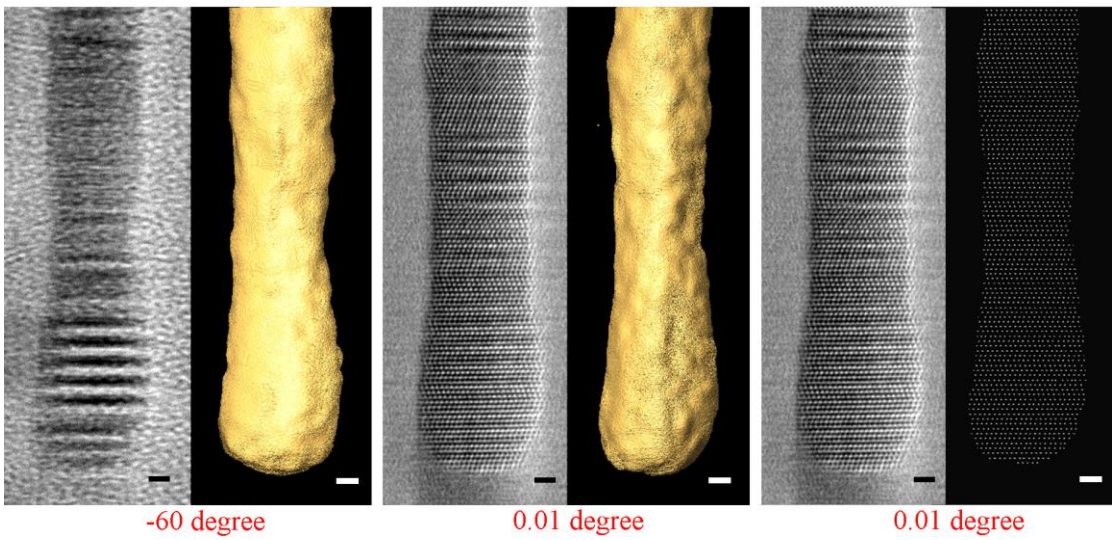

Figures 3.3: Comparisons of two of the tilt series images with the tomographic surface reconstruction (tilt angle -60° and 0°) and the atomic position reconstruction at the 0° tilt image. Holizontal scale marker represents 1nm in length**.**

All 25 images in the aligned tilt-series included (111) lattice fringes, and two of the images (labeled 0.01° and 59.95° in Figure 3.1) were precise on-zone-axis images of <110> atomic columns. Two distinct kinds of information are embedded in tilt-series images: (i) the projected outlines of the nanowire contain all the information about the 3D shape of the wire (see Figure 3.2(b)), and (ii) the two on-zone images contain information about the atomic arrangements within each (111) plane of the sample (Figure 3.2 (a)).

To carry out the surface reconstruction, the 25 tilt-series images were each processed with a Gaussian blur to reduce noise and uneven contrast arising from the supporting amorphous carbon film. An algebraic reconstruction with compressed sensing algorithm was applied to the filtered projections [6], and the reconstructed nanowire volume was segmented using Otsu's method [7] (left branch of the flowchart in Figure 3.4).

The atomic arrangements were extracted from the two on-zone images with a stereo vision approach. The lattice periodicity was reconstructed from [220] and [202] fcc zone-axis images that were first filtered by a radial Wiener filter to reduce the background noise from the amorphous carbon support film. Those two images have epipolar geometry [8], and this made it possible to locate the atoms in the columns using triangulation or simple back projection. This strategy is determinate, and it avoids errors arising from solving traditional

tomography's inverse problem using noisy image data.

Two methods were used to extract the atom positions from the resulting two images. One method consisted of filtered back projection of the on-zone images followed by volume segmentation. On the second method, a peak detection filter was applied to the on-zone images to produce binary-intensity maps of the atomic columns that were then back-projected to locate the atoms. Both methods exploited the epipolar geometry of the on zone projections – which are essentially a set of stereo-pair images – to extract the 3D coordinates of the atoms. The first method reproduces local distortions more accurately, the second is better at reconstructing atomic arrangements in large crystals.

Once the shape and the atomic arrangements were determined, the information was combined to obtain a complete 3D reconstruction with atomic resolution. The surface reconstruction was applied as a mask to the set of atom positions to obtain the full nanowire reconstruction with atomic resolution. The steps in the whole process are summarized in Figure 3.4.

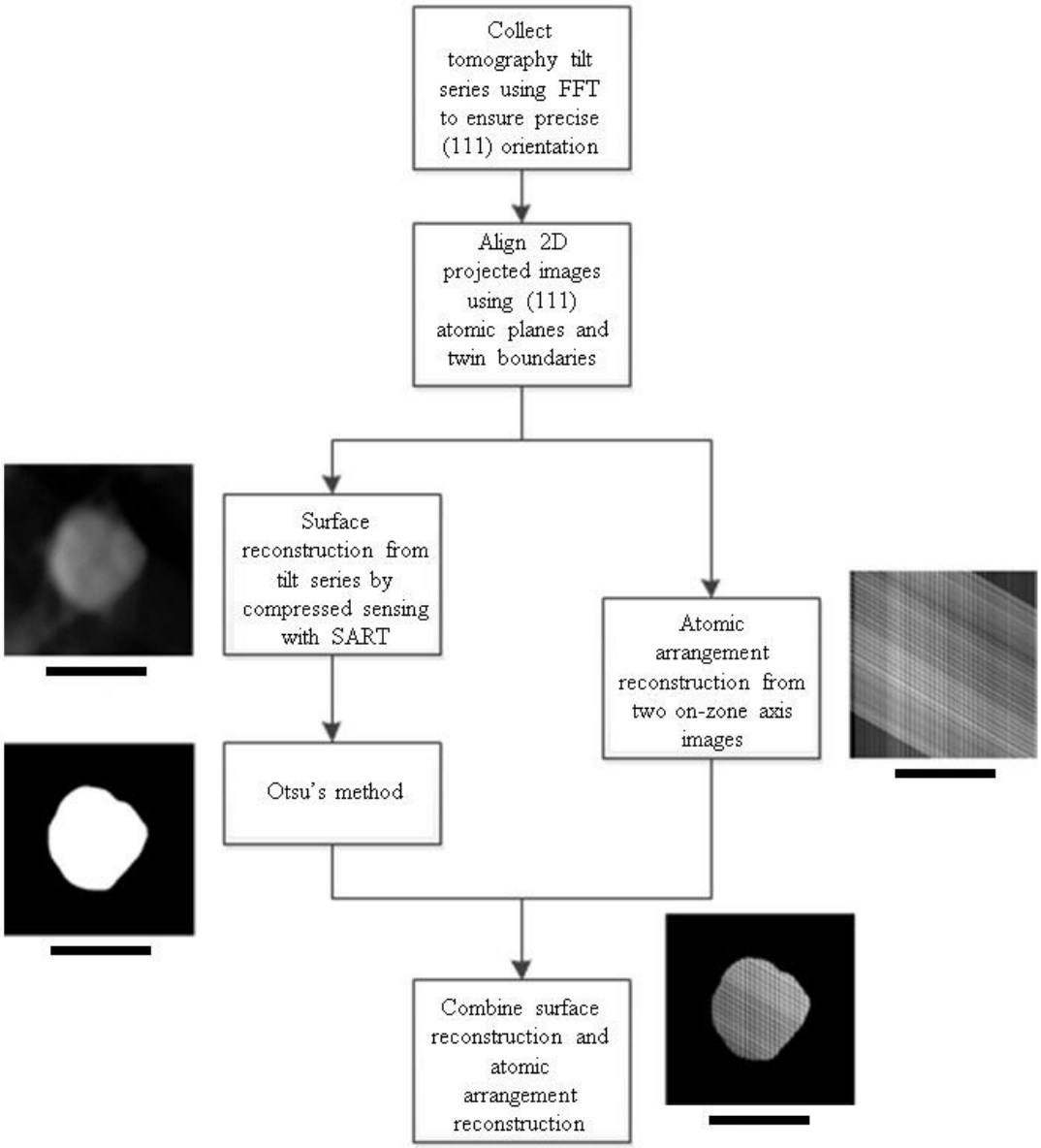

Figure 3.4: Steps in reconstruction procedure; images are cross-sections of the tomographic reconstruction at the corresponding steps Horizontal scale markers represent 5 nm length.

Comparisons between the tomographic reconstruction and tilt series images from which it was derived are made in Figure 3.3 and in Figure 3.5. One of the on-zone projections (Figure 3a) is compared with three different views of a portion of the combined reconstruction (Figures 3.5 (b), (c), and (d)) to demonstrate the fidelity of the reconstruction. The reconstructed region is from the inset box in Figure 3.5 (a). Figure 3.5 (b) is the projection of the reconstruction in the same orientation as image of 3a, Figure 3.5 (c) is the reconstruction

from the other on-zone orientation, and Figure 3.5 (d) shows the reconstruction from an orientation that was not coplanar with the experimental tilt series.

The complex overlapping atomic arrangement of Figure 3.5 (d) arises from the oblique projection direction through the nanowire. Figures 3.5 (b) and 3.5 (c) demonstrate the reconstruction method reproduces the periodicity of the nanowire's fcc crystal structure, but more surprisingly, the aperiodic twin structure also is reproduced faithfully. The cubic symmetry of the selected reconstruction region is clearly evident in the <001> view of Figure 3d, and this demonstrates the 3D reconstruction includes information that is not present in any of the individual images of the tilt-series, because none of them include an <001> zone.

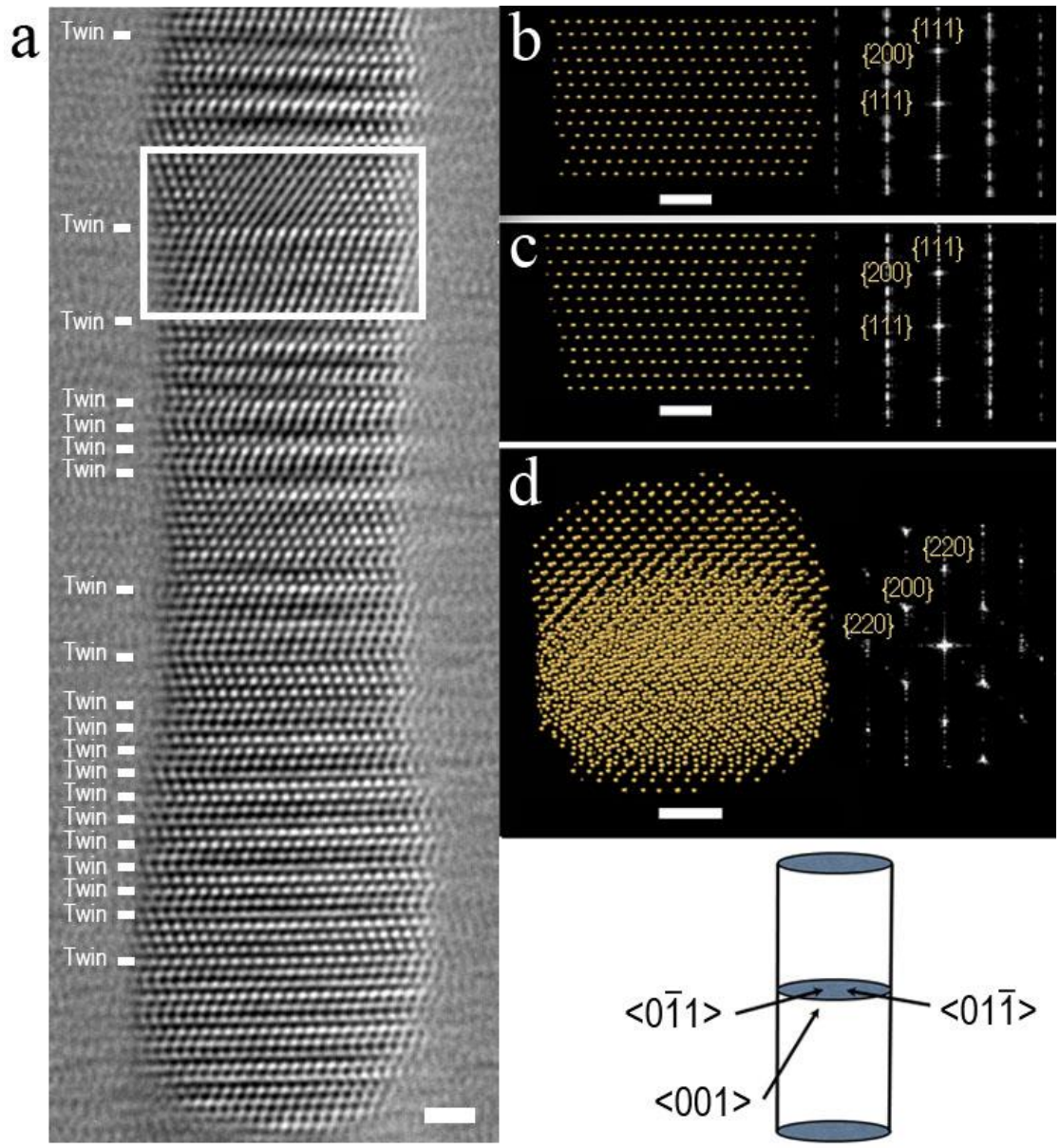

Figure 3.5: Comparison of tomographic reconstruction volume with TEM image. (a)-(d) On-zone HR-TEM image of a gold nanowire (a) showing the locations of twin planes, and projections (b), (c), and (d) of the atoms in the reconstructed volume from the boxed region of (a). The right portion of panels (b)-(d) are Fourier Transforms of the corresponding reconstruction projections; (e) represents the orientation relationship between the three viewing directions of (b), (c), and (d). Horizontal scale markers represent 1 nm length.

The atomic resolution reconstruction demonstrated here provides a vehicle for extracting other structural information that is not readily apparent 2D HR-TEM images. Figure 3.6 (a) is a section of an on-zone projection containing a defect in the plane highlighted by the arrow, and Figure 3.6 (b) is the reconstruction of this plane (viewed from a perpendicular to the plane) showing how atoms (indicated by the black dots) in the lower left region of the plane are systematically displaced from their expected positions in the perfect atomic arrangement (the intersecting lines). The reconstruction provides additional information about dislocation-like features that are unavailable from a single HR-TEM image.

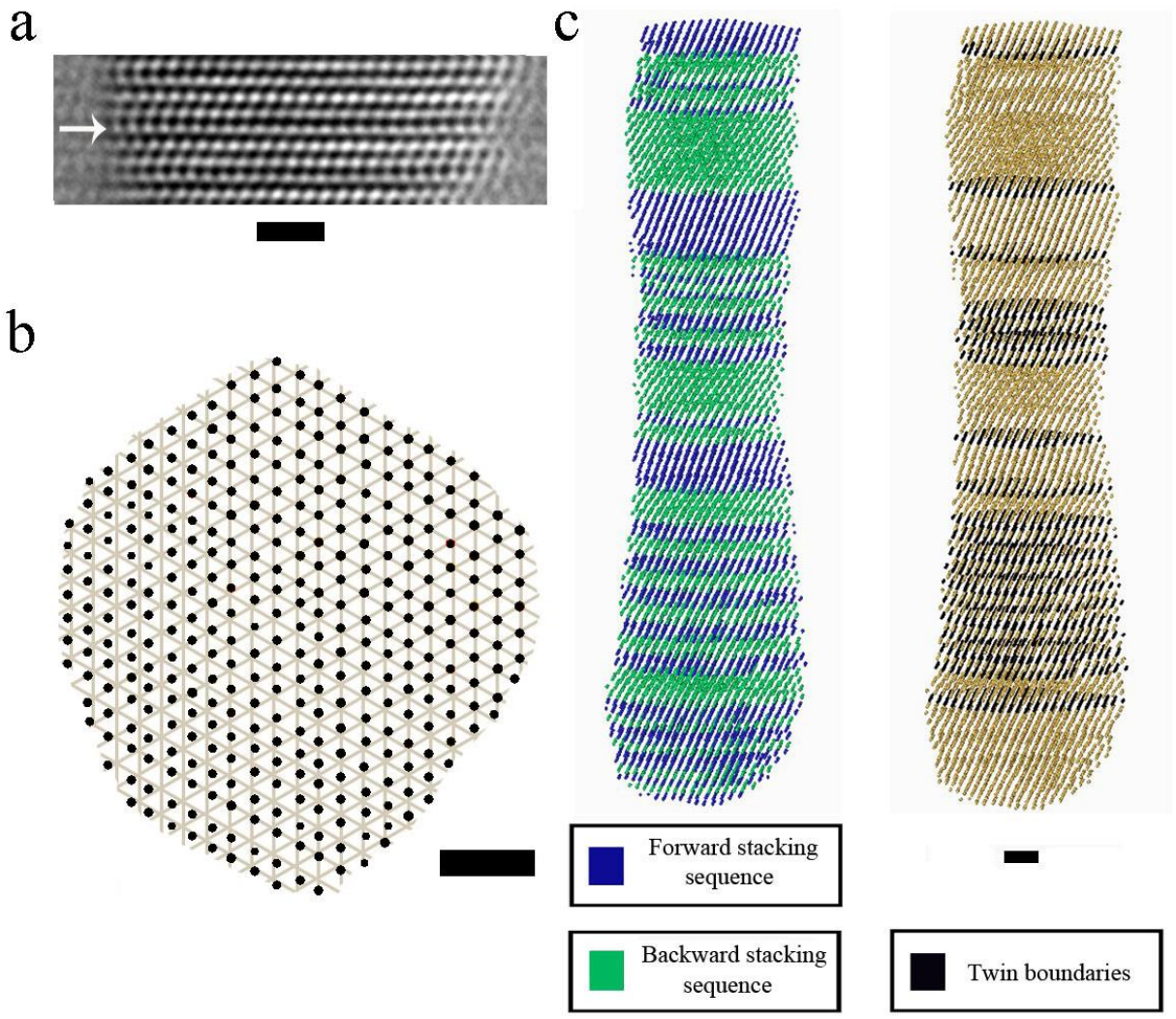

Figure 3.6: Extractable information from 3D tomographic reconstruction. (a)-(c) Anomalous position of the plane labeled by the arrow in on-zone HR-TEM image (a) indicates the presence of a defect. Panel (b) is the atomic arrangement of the corresponding plane from the reconstruction viewed along the perpendicular to plane; the displacement of atom positions (black dots) from the perfect atomic arrangement (the line intersections) in the lower left of (b) suggests the defect in (a) has the character of an extended dislocation. In left portion of panel (c), two twin orientations in the nanowire are colored green and blue, and the boundaries between these twins are highlighted in black in the right portion of panel (c). Horizontal scale markers represent 1 nm length.

The atom positions in the reconstruction also can be used to locate planar defects such as twins and stacking faults. The positions of (111) planes in the gold nanowire reconstruction

were used to identify the (111) stacking sequence, which was then color-coded in figure 3.6 (c) to differentiate between twin boundaries and narrowly-spaced stacking faults. This type of information is important for identifying twinning superstructures [9] that can affect valence band states of compound semiconductor nanostructures and resulting optical properties and electronic transport behavior, or predicting materials strength in quantitative manner [10, 11].

3.3 Summary

In conventional transmission electron microscopy (TEM), the image is taken from two-dimensional (2D) projection of a three-dimensional (3D) object; therefore, the spatial information in third dimension is hidden in 2D micrograph. Without series of image analysis and simulation the 3D spatial information cannot be extracted. One powerful technique to obtain 3D spatial information in TEM is electron tomography. The current highest resolution of electron tomography is 2.4 angstrom. However, even with this resolution the 3D atomic structure of nanoparticles cannot be fully revealed. It is difficult to achieve 3D atomic resolution with electron tomography because the 2D micrographs must be aligned with a spatial accuracy better than the imaged interatomic spacing. Here we demonstrate a model-free stereo vision technique for 3D imaging non-periodic structures containing defects. The technique employs intrinsic crystal features instead of extrinsic fiducial markers to achieve the alignment accuracy needed to reconstruct a crystal with atomic resolution. We apply it to determine the 3D geometry and atomic arrangements of a highly defective gold nanowire.

3.4 Methods

3.4.1 Specimen Preparation

Gold nanowires were chemically synthesized using a procedure similar to Huo et al. [12] and supported on a holey carbon film with a continuous carbon film (Cu-200HD, Pacific Grid-Tech).

3.4.2 TEM Imaging

Tomography tilt series were acquired in the high-resolution TEM imaging mode with an image spherical aberration (Cs) corrected, FEI Titan 80-300 at 300kV. The displayed Cs value was 363 nm. We carefully selected a nanowire for analysis that had its long axis close to the mechanical rotation axis of the sample holder. This choice made it relatively easy to rotate the wire while keeping the (111) planes oriented parallel to the electron beam. A series of images was recorded by tilting the nanowire through a ±60° angular range at approximately 5° intervals. From geometric considerations, lattice fringes from the (111) planes in a 5 nm thick gold wire only appear in the tilt series images if these planes are within 2.7° of the electron beam. By ensuring each image in the tilt series contains (111) lattice fringes, we guaranteed the rotation axis of the series was less than 2.7° away from the normal to the (111) crystal planes.

3.4.3 3D Reconstruction

Each (111) lattice fringe arises from a specific (111) plane in the crystal, and the fringes in each image of the tilt series are thus projections of the (111) planes from different perspectives. To obtain an accurate reconstruction, it is essential to align all the fringes in the tilt series images that arise from the same crystal plane. For the gold nanowire, twin boundaries that appeared in all the images of the tilt series were used, but not limited to this purpose; any intrinsic crystal feature linked to specific atomic planes can be used. Once the corresponding fringes were properly grouped, successive tilt series images were superimposed and their lateral position perpendicular to the (111) traces (the vertical direction in Figure 3.2), was adjusted to maximize an alignment quality index (related to the sum of squared difference in gray-levels) calculated from the cross-correlation of the images. This step was accomplished using the gray values algorithm of the “AlignSlices” function of the FEI ResolveRT software package, and the quality index value 82.3% with the standard deviation 2.04% was obtained. The error in lateral alignment was less than one pixel in the magnified images, which corresponds to less than 0.029 nm calculated from the spacing of the (111) planes. This alignment precision is critical to achieving the atomic-scale reconstruction,

and it is substantially better than what is achievable with external nanoparticle fiducial markers used in traditional tomography reconstructions.

A 2D cross-section at one location along the nanowire illustrating the back-projection step is shown on the right branch of the flowchart in Figure 3.4. The bright intersections in the center of the figure represent the intersections of atomic columns and are atomic positions in the plane of the cross-section through the wire; they are determined directly from the epipolar lines of the two on-zone projections. Any pair of low-index, on-zone images can be used to locate the atoms in a specific atomic plane – regardless of crystal symmetry – provided the atomic columns from the two images lie in the same atomic plane. This condition was met in this experiment by using the twin boundaries to enforce the correct vertical alignment of the (111) traces.

References

[1] J.R. Jinschek, K.J. Batenburg, H.A. Calderon, R. Kilaas, V. Radmilovic, C. Kisielowski, 3-D reconstruction of the atomic positions in a simulated gold nanocrystal based on discrete tomography: Prospects of atomic resolution electron tomography, Ultramicroscopy, 108 (2008) 589-604.

[2] Z. Saghi, X. Xu, G. Moebus, Model based atomic resolution tomography, Journal of Applied Physics, 106 (2009).

[3] S. Van Aert, K.J. Batenburg, M.D. Rossell, R. Erni, G. Van Tendeloo, Three-dimensional atomic imaging of crystalline nanoparticles, Nature, 470 (2011) 374-377.

[4] D. Van Dyck, F.-R. Chen, 'Big Bang' tomography as a new route to atomic-resolution electron tomography, Nature, 486 (2012) 243-246.

[5] M.C. Scott, C.-C. Chen, M. Mecklenburg, C. Zhu, R. Xu, P. Ercius, U. Dahmen, B.C. Regan, J. Miao, Electron tomography at 2.4-angstrom resolution, Nature, 483 (2012) 444-U491.

[6] N. Monsegue, X. Jin, T. Echigo, G. Wang, M. Murayama, Three-Dimensional Characterization of Iron Oxide (alpha-Fe2O3) Nanoparticles: Application of a Compressed Sensing Inspired Reconstruction Algorithm to Electron Tomography, Microscopy and

Microanalysis, 18 (2012) 1362-1367.

[7] N. Otsu, THRESHOLD SELECTION METHOD FROM GRAY-LEVEL HISTOGRAMS, Ieee Transactions on Systems Man and Cybernetics, 9 (1979) 62-66.

[8] Epipolar Geometry in Stereo, Motion, and Object Recognition, a Unified Approach, Kluwer Academic Publishers, Dordrecht, Netherlands, 1996.

[9] R.E. Algra, M.A. Verheijen, M.T. Borgstrom, L.-F. Feiner, G. Immink, W.J.P. van Enckevort, E. Vlieg, E.P.A.M. Bakkers, Twinning superlattices in indium phosphide nanowires, Nature, 456 (2008) 369-372.

[10] J.R. Greer, J.T.M. De Hosson, Plasticity in small-sized metallic systems: Intrinsic versus extrinsic size effect, Progress in Materials Science, 56 (2011) 654-724.

[11] X. Li, Y. Wei, L. Lu, K. Lu, H. Gao, Dislocation nucleation governed softening and maximum strength in nano-twinned metals, Nature, 464 (2010) 877-880.

[12] Z. Huo, C.-k. Tsung, W. Huang, X. Zhang, P. Yang, Sub-two nanometer single crystal Au nanowires, Nano Lett., 8 (2008) 2041-2044.

Chapter 4

A Software Tool for Automatic Analysis of Selected Area Diffraction Patterns within Digital Micrograph

4.1 Background

Selected area diffraction patterns (SADP) taken with transmission electron microscopes are widely used to analyze crystal structure. To perform a precise analysis of a SADP, one has to determine accurately the location of the forward-scattered spot, which is the origin of reciprocal space for the pattern, the location of individual diffraction spots, and/or the locations of diffraction rings.

Several software packages are available for doing portions of these operations on digital images. Diffraction rings from polycrystalline samples can be analyzed automatically with software that utilizes a circular Hough transform [1]. Programs that locate the forward-scattered beam in single crystal diffraction patterns or the positions of the diffraction spots, however, are not automated and have some limitations. Most of these programs require some manual intervention or a centrally symmetric pattern to function well [1,2,3,4,5,6,7,8,9,10] .

There are five methods for locating the forward-scattered spot on a diffraction pattern. The “center-of-gravity” [2] and cross-correlation [5] methods can reliably identify the location of this spot if the whole diffraction pattern is symmetric about the spot. A third method identifies the forward-scattered spot as the intersection point of two lines manually drawn through two sets of +g , –g diffraction vectors. A fourth method is to subjectively pick the center spot with a mask of rings. The last method is to index three diffraction spots and use the positions and indices of those three spots to calculate the position of forward-scattered spot [8,9,10]. None of these approaches are easily automated because they require a user to

manually select a region of the diffraction pattern for analysis. Furthermore the first four methods may not be highly accurate when the diffraction pattern is not centrosymmetric about the forward scattered spot.

As far as finding the centers of diffraction spots are concerned, the center-of-gravity method is the most common approach. The user draws a box around the diffraction spot to be located, and the software then finds the coordinates of the spot by calculating the center of gravity of the diffraction intensity. This method has several limitations, though. If a diffraction pattern includes a lot of background noise, as is common when the pattern is a fast-Fourier transform (FFT) of a high-resolution TEM image, or if the diffraction pattern is not symmetric, the center-of-gravity algorithm tends to be inaccurate. The latter situation is common when the incident electron beam is tilted away from an exact zone axis or when microstructural features introduce rel-rod streaks. For these cases, an alternate algorithm for locating the center of the pattern and the diffraction spots is desirable.

In this letter, we describe an algorithm that is not subject to the limitations of the center-of-gravity method. The algorithm iterates a cross-correlation of a circular mask with a diffraction pattern to sharpen the diffraction intensities; the coordinates of the sharpened diffraction peaks are then found by searching for the maximum intensity. The approach is convenient for locating the centers of the forward scattered beam and the diffracted spots simultaneously and in an automated fashion. The algorithm has been implemented in a software tool called AutoSADP, which is written as a plug-in script for Digital Micrograph [11,12,13]. The AutoSADP tool is designed to be user-friendly, and when it is run in an automatic mode, it locates diffraction peaks reliably with little prior knowledge on the part of the user. Other features are available in AutoSADP to calculate interplanar angles and d-spacings, and these data can be applied to search the powder diffraction database, PDF-2 [14], or used to search for phases in relational database like ZONES [15].

4.2 Algorithm

The first step in the procedure involves modifying the shape of the diffraction spots in the SADP. Diffraction spots can be circular or irregular in shape, and their intensity distribution may or may not be radially symmetric. In many cases, the intensity in recorded

diffraction pattern saturates over a significant fraction of a diffraction spot's area and some wild intense intensity pixels may be caused by x-ray. These characteristics make it impossible to locate a diffraction spot from the maximum intensity. Narrowing and sharpening the intensity distribution of the diffraction spots can circumvent this problem.

The simplest way to reliably accomplish this is to apply a cross correlation between a circular mask and the whole diffraction pattern. If the intensity distribution over the diffraction pattern is represented by *g(x,y)*, and a circular mask (with a transmission "hole" roughly the size of the diffraction spots in the pattern) is represented by *f(x,y)*, then the cross correlation of f on g is a two-dimensional function,

$$c(x,y) = f(x,y) \bigstar\bigstar g(x,y) \qquad (1)$$

that has the effect of converting broad, flat-topped diffraction intensities in the image *g(x,y)* to narrower, peaked functions in *c(x,y)*. Figure 1 shows a two-dimensional example of this transformation. Figure 1(a) is an idealized diffraction spot consisting of a disk 21 pixels in diameter with uniform intensity; this corresponds to an image function, *g(x,y)*. Figure 1(b) represents the intensity profile along the horizontal line in Figure 1(a). The function *f(x,y)* is taken to be a circular mask also 21 pixels in diameter. The cross correlation is shown in Figure 1(c) and the intensity distribution through the transformed spot is shown in Figure 1(d). Note how the broad diffraction disk in 1(a) has been replaced with the peaked function in 1(d) whose maximum is located at the center of the original disk.

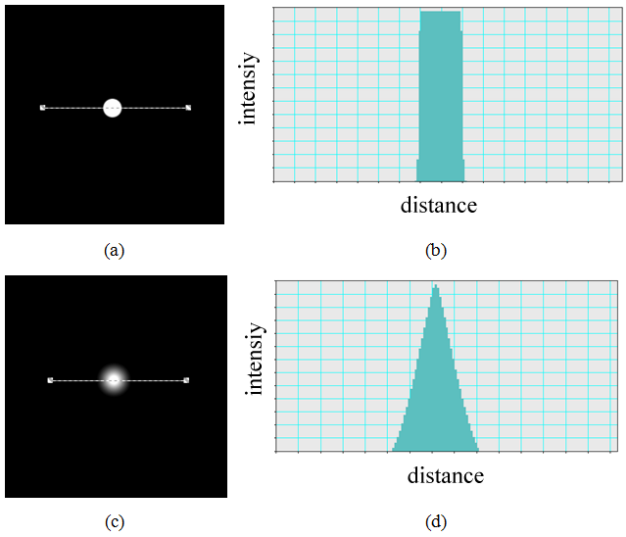

Figure 4.1: (a) Spot with diameter of 31 pixels (b) Intensity profile along the line through the

spot (c) Image of spot after one convolution (d) Intensity profile after one convolution

Cross-correlating a circular aperture on diffraction spots sharpens diffraction spots (gives them a peak intensity) in binary white/black images, but it can introduce extraneous spots in experimental patterns with non-zero background intensities. Artifacts of this type are easily avoided by first applying a threshold filter [16] to experimental images to remove extraneous intensity from inelastically scattered electrons.

Many experimental patterns include diffraction spots of very different sizes. To treat these cases, the cross correlation transform can be applied iteratively. Each successive cross correlation sharpens and narrows the disks further until a central maximum eventually appears in the largest diffraction disk (usually the forward scattered beam). The intensity distribution in small diffraction spots also becomes narrower and sharper with successive transforms, but the positions of the central maxima do not change.

Once the iterations produce a peaked intensity distribution in the largest diffraction disk, the locations of all the spots are identified as the coordinates of all the local intensity maxima. Finally, d-spacing and interplanar angles are calculated from the detected locations of the diffraction spots and the forward scattered spot and the pixel size. The whole algorithm is summarized in the flow chart of Figure 2.

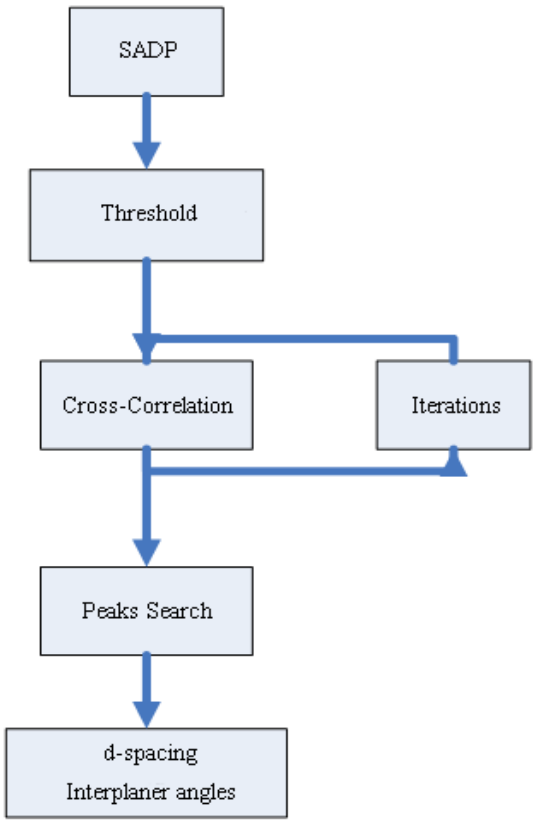

Figure 4.2: Algorithm for detecting diffraction disks and locating their centers

4.3 Method Accuracy and Applications

4.3.1 Simulated Data Analysis

To evaluate the accuracy of the new algorithm, several simulated diffraction spots were analyzed with the program, AutoSADP. These included an ideal diffraction spot, a centrosymmetric diffraction spot with uniform background noise, an off-center diffraction spot with noise, and a noisy asymmetric diffraction spot. The ideal diffraction spot was generated using Equation 2, which gives the theoretical intensity profile through a diffraction spot [17] where t is the specimen thickness, S_{eff} is the effective excitation error, and ξ_g is the extinction distance.

$$I_g=\left(\frac{\pi t}{\xi_g}\right)^2 \frac{sin^2 \pi t S_{eff}}{\pi t S_{eff}} \qquad (2)$$

The relative intensity versus a normalized reciprocal distance for the ideal spot is

plotted in Figure 3(a). Similar intensity versus reciprocal distance plots for the other simulated diffraction spots are shown in Figures 3(b-d): Figure 3(b) is the case of the centrosymmetric diffraction spot with uniform noise, Figure 3(c) is the off-center (but still symmetric) diffraction spot with uniform noise, and Figure 3(d) is a slightly asymmetric diffraction spot that was generated using non-uniform noise. The noise was generated from the background of an FFT of a high-resolution TEM image. The locations of the centers of the simulated spots (which are known exactly) were calculated using the center of gravity method and the iterated cross-correlation method for comparison. The errors obtained by the two approaches are summarized in Figure 3(e).

It is evident from Figure 3(e) that both methods yield an error of approximately 2% or less when the diffraction spot is centrally located (the cases shown in Figures 3(b) and (d)). However, the error associated with the center of gravity method is greater than 5% when the simulated diffraction spot is off-center (Figure 3(c)). In a practical sense, this means the center of gravity method does not work well unless the diffraction spot of interest is positioned precisely in the center of the analysis box used by the software. On the other hand, the cross-correlation method remains accurate to within about 2% for all the simulated cases that include noise.

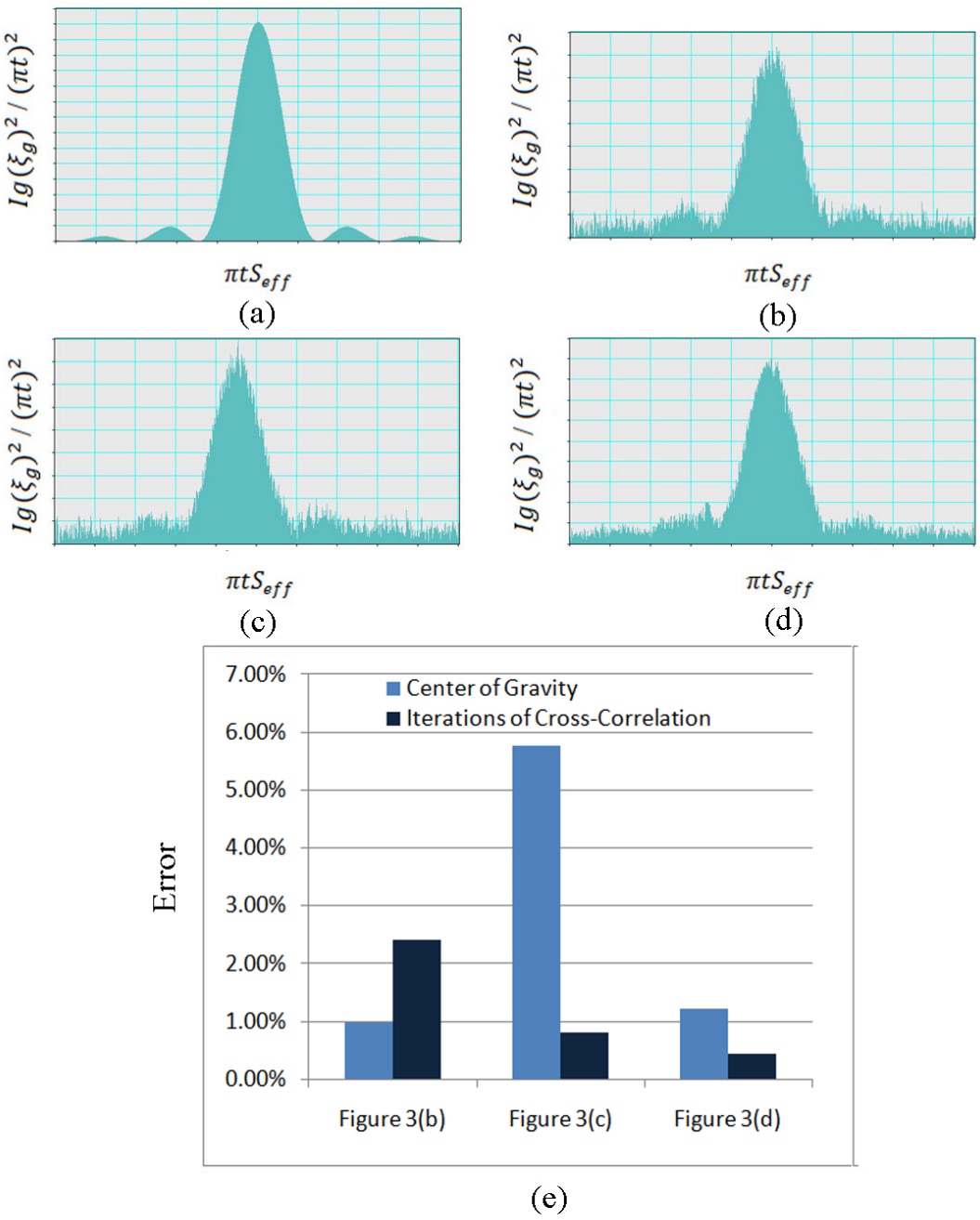

Figure 4.3: (a) Theoretical Intensity Distribution of Diffracted Beam (b) Centrosymmetric Diffracted Beam Intensity with Uniform Noise (c) Off-Center Centrosymmetric Diffracted Beam Intensity with Uniform Noise (d) Centrosymmetric Diffracted Beam Intensity with Non-uniform Noise (e) Comparison chart of the detected center by two methods

4.3.2 Experimental Data Analysis

Several experimental SADPs taken from different single crystal samples were tested with AutoSADP. Figure 4(a) is a [001] oriented single crystal aluminum SADP scanned from film. The diffraction spots in Figure 4(a) are all approximately circular but different in size if a certain threshold is given. The results at various stages of AutoSADP algorithm are shown in Figure 4(b)-(d). The intensity profile along the dashed line in diffraction pattern of Figure 4(a) is shown in Figure 4(b). The intensity after the background subtraction is shown in Figure 4(c). After the 7th iteration, each diffraction spot has a local maximum at a single point in the intensity profile which is shown in Figure 4(d).

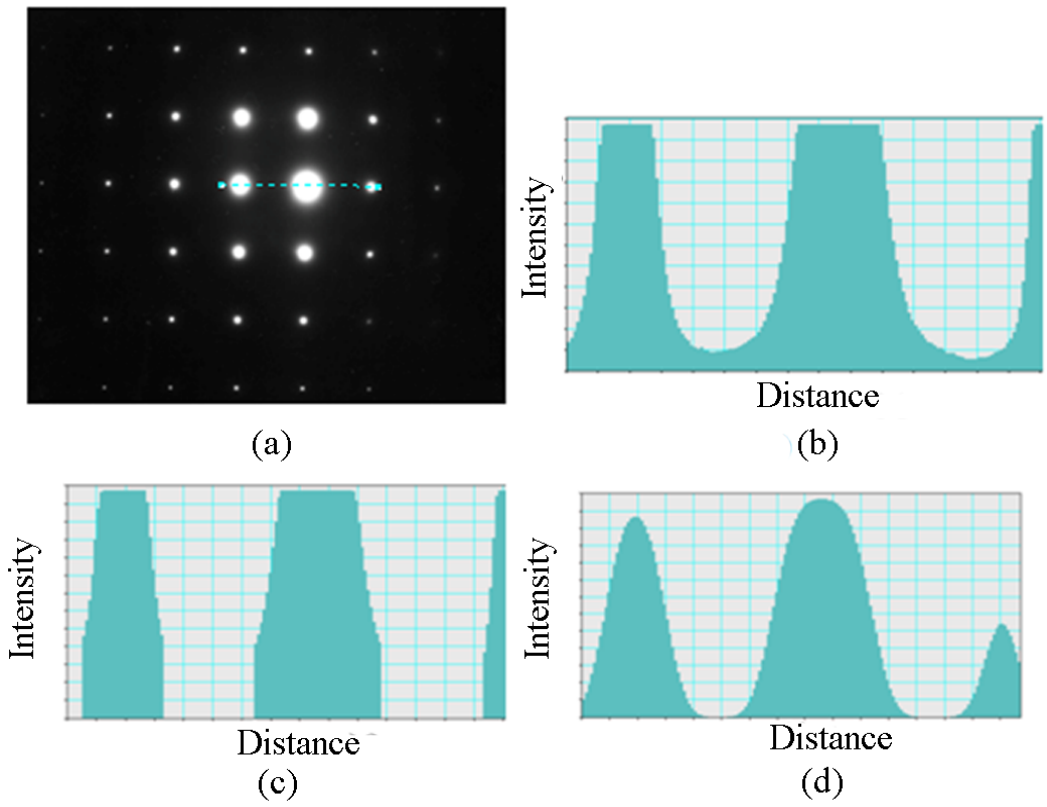

Figure 4.4: (a) Original Selected Area Diffraction Pattern(SADP) (b) Original Intensity Profile Along the Line in SADP (c) Filtered Intensity Profile (d) Intensity Profile After 7th Iteration of Cross-Correlation

Two types of pattern which can be difficult to analyze with automated software are treated in Figure 5. Figure 5(a) is an FFT of a high-resolution TEM image from gold [8]. The

iterated cross-correlation technique converts the original intensity profile from the FFT pattern (Figure 5(c)) to the smoother version shown in Figure 5(d). The locations of the spots determined by the AutoSADP routine are shown superimposed on the original FFT in Figure 5(b). The final panel of Figure 5 demonstrates the AutoSADP algorithm locating the primary diffraction spots in a streaked diffraction pattern from Ni_2MnGa. The algorithm works well despite the presence of pronounced streaks in the diffraction pattern, (Figure 5(e)).

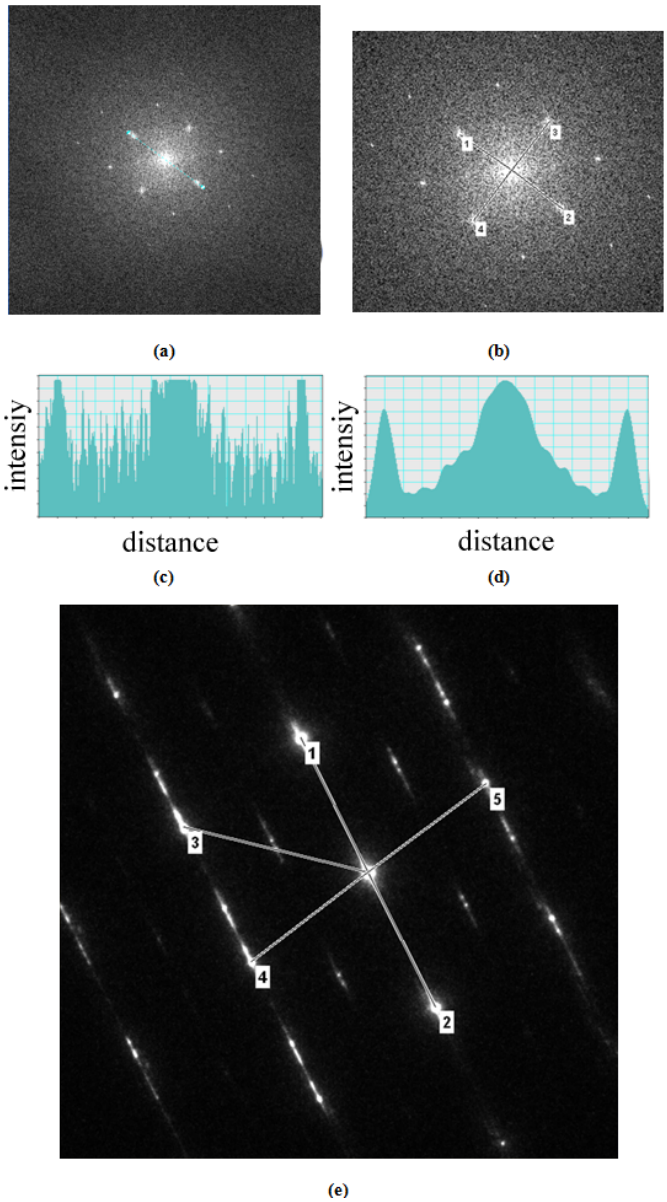

Figure 4.5: (a) FFT from high-resolution image of gold, (b) automatic detection of FFT diffraction spots, (c) intensity profile through FFT diffraction spot, (d) intensity profile through FFT spot after iterated cross-correlation, and (e) automatic detection of diffraction

spots in a pattern with pronounced streaking.

The overall accuracy of AutoSADP measurements were tested using a [001] gold single crystal. Errors in the ratios of reciprocal lattice vectors were less than 0.5% and errors in measured interplanar angles were 1.89%. These errors may due to excitation errors and lens distortion [18] and are well within the 1-2% measurement errors typically expected from calibrated TEM diffraction patterns [17].

Although the AutoSADP software is intended to identify diffraction spot locations without user intervention, it has some limitations. First, AutoSADP assumes the largest and brightest diffraction spot is the forward-scattered beam; there are conditions, albeit unusual, when this is not the case. Second, the program's default parameters (for cross-correlation and other operations), were selected by observing what worked best for many different types of diffraction patterns; but they will not work for all kinds of patterns. The parameters can be adjusted as needed to improve the program's performance for diffucult patterns. For example, if the diffraction spots are especially small, the diameter of circular mask used for the cross-correlation can be reduced accordingly. Third, the program has capability of locating overlapped points; however, if the region between centers of two overlapped diffraction spots is saturated the program may not locate these two spots correctly; therefore, users should set acquisition condition to eliminate saturation. At last, the beam stop is often used to prevent forward-scattered beam from damaging the CCD camera. Those diffraction patterns with beam stop cannot be automatically analyzed by the software, AutoSADP, because the center spot cannot be located automatically. However, by applying the iterated cross-correlation method the diffraction spots can still be indentified automatically.

4.4 Software Package: SADP Tools

The software package "SADP Tools" [19] provides complementary diffraction pattern analysis tools for use with AutoSADP. SADP Tools includes 5 programs: AutoSADP, Manual SADP, Auto I- Extractor, Pixel Size Calc and Scale Bar Calc. AutoSADP automatically analyzes diffraction patterns from single crystals. Manual SADP is designed to analyze diffraction patterns that are not amenable to automatic analysis with AutoSADP such as ring

patterns from polycrystals or patterns with beam stop. Auto I-Extractor which also applies iterations of cross correlation method can be applied to extract intensity profiles of diffraction spots automatically. Pixel Size Calc enables users to determine the diffraction pattern pixel size (which is equivalent to the pattern magnification) from an accurately known d-spacing. Scale Bar Calc is useful for calculating pixel size when the diffraction pattern includes an accurate scale bar.

4.5 Summary

A software tool called AutoSADP is described that facilitates automated measurements of d-spacing and interplaner angles from TEM selected area diffraction patterns (SADPs) of single crystals. The software uses iterative cross correlations to locate the forward scattered beam and find the coordinates of the diffraction spots. The algorithm is suitable for automated analysis and it works well with asymmetric diffraction patterns, off-zone axis patterns, patterns with streaks, and noisy patterns generated from Fast Fourier Transforms of high-resolution images. The AutoSADP tool runs as a macro for the Digital Micrograph program and can generate d-spacing values and interplanar angles with an accuracy of better than about 2%.

References

[1]D.R.G. Mitchell, Circular Hough transform diffraction analysis: A software tool for Automated measurement of selected area electron diffraction patterns within Digital MicrographTM, Ultramicroscopy 108(2008) 367-374

[2] D.R.G. Mitchell,DiffTools: Electron Diffraction Software Tools for Digital MicrographTM, Microscopy Research and Technique 71(2008) 588-593

[3] J.L. Labar, Consistent indexing of a (set of) single crystal SAED pattern(s) with the Process Diffraction program, Ultramicroscopy 103(2005) 237-249

[4] Digital Micrograph TM Script Database, <http://www.felm

i-zfe.tugraz.at/dm_scripts/dmscript1.html >,2011

[5] DIFPACKTM, < http://www.gatan.com/products/digital_imaging/products/difpac.php >, 2011

[6] D. Belletti, G. Calestani, M. Gemmi, A.Migliori, QED V 1.0: a software package for quantitative electron diffraction data treatment, Ultramicroscopy 81(2000) 57-65

[7] D. Vincent, H. Hou, A DigitalMicrograph^{TM} Script to Characterize Elliptical Distortion of Electron Diffraction Patterns in TEM, Microsc Microanal 14(Suppl 2), 2008,p.1124

[8] S. Hovmoller, CRISP: crystallographic image processing on a personal computer , Ultramicroscopy 41(1992) 121-135

[9] X. Zou, Y. Sukharev, S. Hovmoller, ELD – a computer program system for extracting intensities from electron diffraction patterns, Ultramicroscopy 49(1993) 147-158

[10] X. Zou, Y. Sukharev, S. Hovmoller, Quantitative electron diffraction – new features in the program system ELD, Ultramicroscopy 52(1993) 436-444

[11] Digital MicrographTM, <http://www.gatan.com/scripting/d ownloads.php>, Gatan Inc., Pleasanton, CA,2011

[12] D.R.G. Mitchell, B. Schaffer, Scripting-customised microscopytools for Digital MicrographTM , Ultramicroscopy 103(2005) 319-332

[13]Digital Micrograph Script Function, < http://www.felmizfe.tugraz.at/dm_scripts/dm_scripts/AddInfo/Old-DMHelp/A llFunctions.html >, 2011

[14]Powder Diffraction Data Base, < http://www.icdd.com >,2011

[15]H.V. Hart, ZONES: a search/match database for single-crystal electron diffraction, Appl.Cryst 35(2002)552-555

[16]J.C. Russ, The Image Processing Handbook, fifth ed. CRC Press, New York,2006

[17] D.B. Williams, C.B. Carter,Transmission Electron Microscopy, second ed., Springer , New York,2006, p.228,p. 304

[18] G.C. Capitani, P. Oleynikov, S. Hovmoller, M. Mellini, A practical method to detect and correct for lens distortion in the TEM,Ultramicroscopy 106(2006) 66-74

[19] SADP Tools,< http://www.ictas.vt.edu/facilities/ncfl.shtml>

Chapter 5

Nanowire Growth Rate and Morphology Evolution of Platinum Nanocrystals Controlled by Reaction Time and Temperature

5.1 Background

Platinum nanocrystals present unique optical, chemical and magnetic properties [1-4] rather than their bulk counterpart. These unique properties lead platinum nanocrystals in applications such as surface enhanced Raman scattering, oxygen reduction in proton exchange membrane fuel cell and ferrofluid.[2, 3, 5-9] Therefore researchers are interested in factors that affect these properties in the platinum nanocrystals. Besides the extensive studied size effect, it has been reported that many chemical and physical properties are morphology dependent.[1, 10, 11] For example, platinum dendrites and platinum sphere have different catalyst activities which result in different amounts of decreases in activation energy for reduction of ferricyanide by borohydride.[12] Moreover, branched platinum nanoparticles were reported to have higher magnetization than spherical nanoparticles.[5] Thus, achieving synthetic control of morphology of platinum nanocrystals is important for tuning their properties.

In last decade, many methods for morphology control of platinum nanocrystals have been developed.[1, 5, 7, 13-15] However, only small amount of these methods focuses on fabrication of single crystal platinum nanowire.[13] Some of these limited methods for nanowire fabrication rely on substrate such as carbon powder or carbon nanotube to promote the nanowire growth.[16, 17] Some others rely on other metallic ion to trigger nanowire growth in reaction solution. For instance, iron ions can be added to reduce platinum ion reduction in polyol process and facilitate the nanowire growth.[13] Therefore, all these synthesis require either special setup of substrate or multiple processing steps. A simple

one-step one-pot method[2] would be desired for simplifying synthesis routine of nanowire fabrication.

Here we present a one-pot method for fabrication of single crystal platinum nanowires. Our synthesis method only consist one metal precursor and one surfactant. During our synthesis, platinum nanocrystals were sampled at four different reaction times and temperatures to monitor the nanowire growth and morphology evolution. Morphology of synthesized platinum nanocrystals was characterized by transmission electron microscopy (TEM). Not only nanowires were found but also nanodnedrites[4, 15, 18, 19] and nanoflowers[18] were found as by-product in our synthesis. Besides the morphology, the preferred growth orientaioin of nanowires were determined to be <111> orientation by high-resolution transmission electron microscopy. The growth rate of the nanowires to the reaction temperature were plotted and further fitted with Arrhenius equation as a model. With the developed model, the morphology of nanocrystals can be predicted.

5.2 Results and Discussion

Total of sixteen samples were prepared in this experiment to investigate the nanowire growth and morphology evolution in platinum nanocrystals. The synthesis condition of reaction temperature and time in Log form of each sample was illustrated in Figure 5.1 (a). The morphology of the samples was characterized by conventional TEM bright field (BF) imaging. Figure 5.1 (b) shows BF images of the samples marked with numbers which refer to respective synthesized condition in Figure 5.1 (a). Based on the observation of the BF images in Figure 5.1 (b), nanowires were always found in platinum nanocrystals regardless of reaction temperature; moreover, these nanowires lengthen as the reaction time increases. Moreover, nanodendrites and nanoflowers were also observed in our platinum nanocrystals. The nanodendite appeared at 250℃ with reaction times of 5 min and 8min. The nanoflowers formed at 250℃ with reaction time of 13 min and at 230℃ with reaction time of 21min. This TEM study shows that by vary reaction time and temperature platinum nanocrystals can form various morphology. Both energy dispersive spectroscopy (EDS) and conventional selected area electron diffraction (SAED) patterns confirms that the nanocrystals were pure platinum

with the fcc structure.

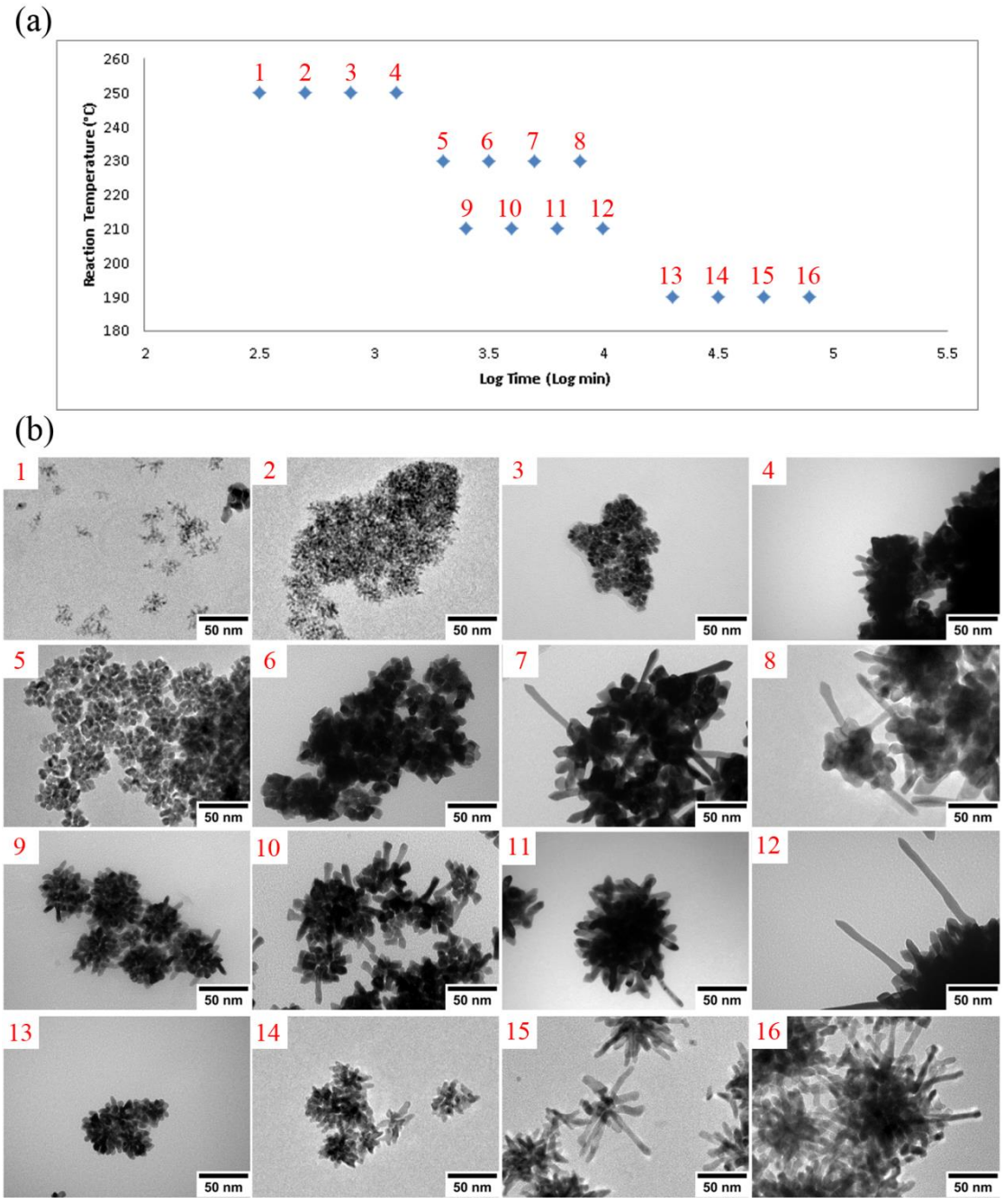

Figure 5.1: (a) A plot of reaction temperature and Log time of chemical synthesized conditions of platinum nanocrystals. (b) TEM bright field images of the synthesized platinum nanocrystals. Number in each image refers to respective synthesized condition in (a)

To determine the growth orientation of the platinum nanowires, HRTEM was utilized to analyze the atomic structure of the nanowires. Figure 5.2 (a) shows a HRTEM image of a

platinum nanowire. The spot pattern in the Fast Fourier Transform (FFT) in Figure 5.2 (a) indicates that the nanowire is single crystal; moreover, the growth orientation of the platinum nanowire was further determined to be <111> by analyzing the FFT. The tip of nanowire was observed to be faceted with {200} and {111} planes as shown in Figure 5.2 (a). To interpret the observed faceted tip we enclosed an end of single crystal platinum nanowire with low energy {111} surfaces and then the tip formed a tetrahedral as shown in Figure 5.2 (b)[20, 21]. If we viewed a simulated atomic structure of the tetrahedral tip from $[1\bar{1}0]$ zone axis, the structure of the tip also forms facets with {200} edge and {111} plane as shown in 5.2 (c). This result matches with the HRTEM in Figure 5.2(a). This indicates that these faceted tips of experimental platinum nanowires were likely to be enclosed with {111} planes.

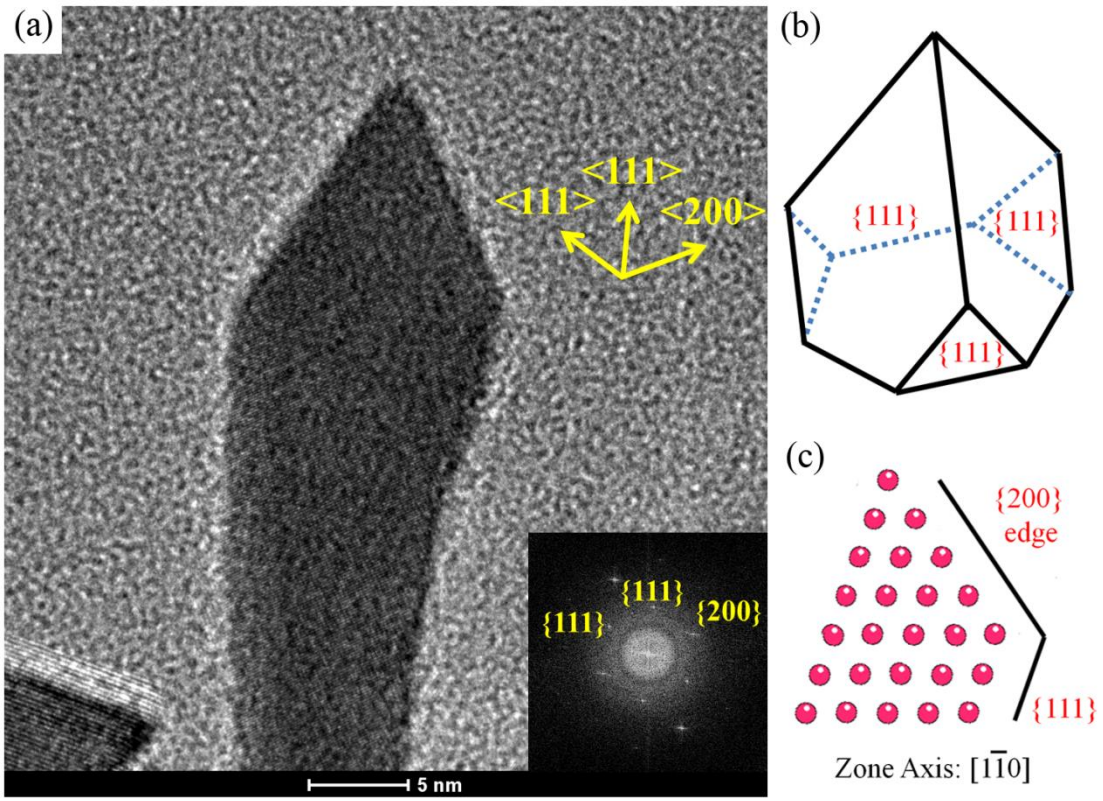

Figure 5.2: (a) HRTEM image of single-crystal platinum nanowire. (b) An end of single-crystal platinum nanowire can be enclosed with {111} surfaces and forms a tetrahedral tip. A atomic structure of a tetrahedral tip viewed from $[1\bar{1}0]$ zone axis.

From the results shown above, we conclude the growth of our platinum nanocrystal in a

schematic illustration in Figure 5.3. Unlike seeded-growth[2], our chemical synthesis is a one-pot method[2]; thus, it requires formation of seeds at the beginning of chemical synthesis to serve as nucleation sites for adatoms to attach. Therefore, only equiaxed platinum nanocrystals were observed at the early stage of our chemical synthesis. Also in this stage nanodendrites and nanoflowers [4, 15, 18, 19] were observed. Once initial seeds were formed, enough nucleation sites presented and anisotropic growth start taking place. The nanowires start to form and grow along a <111> orientation as reaction time increases. This one-dimensional nanowire growth can be leaded by the ligand assisted growth model or the template growth model.[22-25] It has been reported that surfactant, oleylamine,[23] which was utilized in this experiment plays important role in these models and it can promote one-dimensional nanowire growth in a <111> orientation. The tips of nanowires were found to be faceted and these facets can be due to enclosure of {111} surfaces on the tips of the nanowires.[20] It is known that {111} surface has lowest surface energy among all other low-index planes in fcc metals. Therefore this formation of {111} surfaces enclosed tetrahedral tip can be considered as surface energy minimization of platinum nanowire growth front.

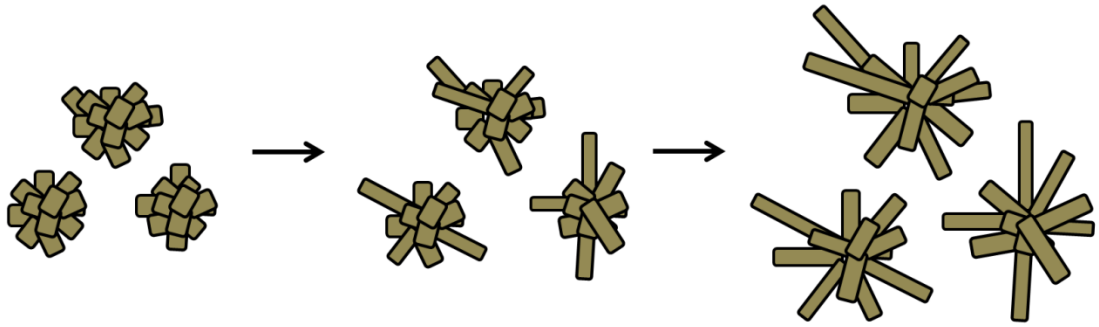

Figure 5.3: Illustration of general growth of platinum nanocrystals in the chemical synthesis.

It has been reported that catalyst activity and surface induced plasmon resonance are morphology dependent; therefore, morphology control such as lengthening in nanowire is important. Based on the measurement of the lengths in the nanowires observed by bright field imaging, the length of the platinum nanowire versus time was plotted in Figure 5.4 (a) to (d). Figure 5.4 (a) and (b) represent the data of the nanowires grown at 190 °C and 210 °C. Both

data show good fitting with linear function. This means that growth rate is generally time independent. Since several data points indicated zero growth of nanowires at reaction temperatures of 230 °C and 250 °C, there are less data points for linear fitting in 5.4 (c) and (d). The growth rates of platinum nanowires at each reaction temperature were measured by the slopes of the linear fittings. The growth rates were then plotted with temperature in Figure 5.4 (e) and the data points were fitted with an exponential equation. Figure 5.4 (e) shows that growth rate increase exponentially with reaction temperature. At last we apply Arrhenius equation to model temperate dependent growth rate in platinum nanowires in Figure 5.4 (f). The R squared value of 0.9677 indicates that the fitting of Arrhenius equation with our data points is reasonably well. Finally, with the fitted model, the growth rate of nanowire can be predicted by reaction temperature and the length of platinum nanowires can be controlled by adjusting reaction time and temperature.

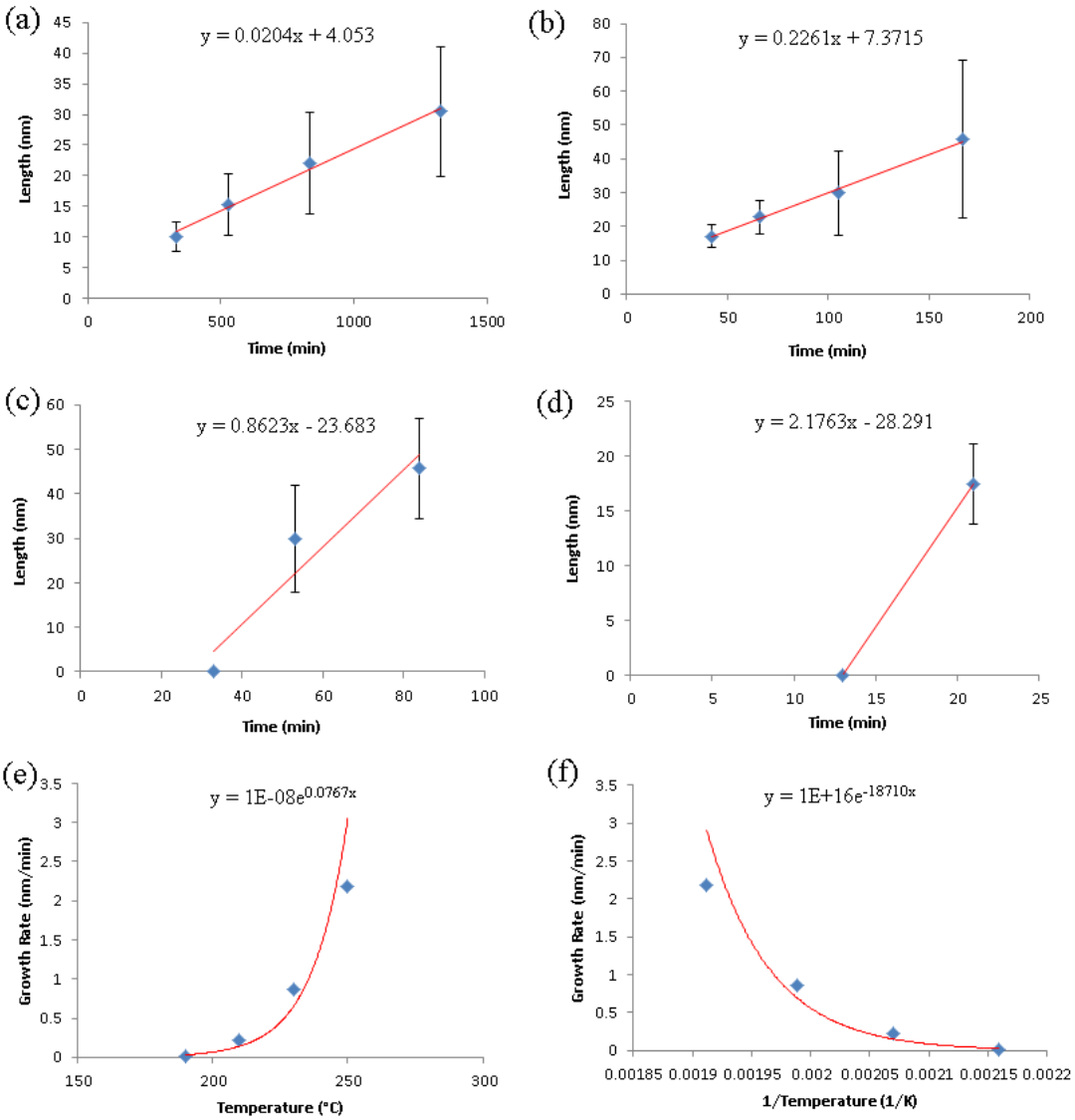

Figure 5.4: A plot of length of platinum nanowire versus time at (a) 190 °C, (b) 210 °C, (c) 230 °C and (d) 250 °C. (e) A plot of growth rate versus temperature of platinum nanowire. (f) A plot of growth rate versus reciprocal of temperature of platinum nanowire.

5.3 Summary

Morphology control of platinum nanocrystals has gained great attentions in last decade because it can bring another meaning in tuning physical and chemical properties of the nanocrystal. In this investigation, we presented a simple solution-phase chemical synthesis with controls of reaction temperatures and times which can lead to morphology evolution of nanodendrites, nanoflowers, and nanowires in platinum nanocrystals. The transmission

electron microscopy (TEM) was used to characterize structure and morphology of the platinum nanocrystals. Our synthesized platinum nanowires were found to have single crystal structure and preferred growth orientation of <111> crystallographic direction by high-resolution transmission electron microscopy (HRTEM). The growth rate of the platinum nanowires to the reaction temperatures was modeled with Arrhenius equation. With the fitted model the growth rate of platinum nanowires can be predicted by reaction temperature. This can lead to precise control of morphology of synthesized nanocrystals.

5.4 Methods

5.4.1 Chemical Materials

Chloroplatinic acid (as an 8 wt% solution in H_2O, Sigma-Aldrich) was used as precursor. oleylamine (70%, Sigma-Aldrich) served as surfactant, reducing agent, and solvent. Ethanol (100%) was used to remove the excess surfactant on nanoparticles. Hexanes (reagent isomers, >98.5%) was used to disperse nanoparticles to become suspension.

5.4.2 Controlled Synthesis of Pt Nanocrystals

Platinum nanocrystals were prepared by solution-phase chemical synthesis derived from prior works.[22, 26] First of all, 0.4 mmol of chloroplatinic acid (as an 8 wt% solution in H2O, Sigma-Aldrich) and 40 mL of oleylamine were mixed in a 100 mL round-bottom three-necked flask. Afterward, the flask was connected to a Schlenk line and the mixed solution was flushed with argon for 15 minutes with magnetic stirring. The solution was heated to 60 ℃ by heating mantle for 20 minutes to mix the yellow reaction solution under argon flow. Once the solution is fully mixed the magnetic stirrer was turned off to eliminate possible mechanical disturbance which night result in defects nanocrystal. Four mixed solutions were prepared separately and then heated to 190℃, 210℃, 230℃ and 250℃ respectively at a rate of 3 ℃ per minute. At each temperature, four samples (10 ml solution) were taken out from reaction flask by a syringe individually at different reaction time to observe the growth process of platinum nanocrystals. The reaction time periods for each

sample taken were listed as follows. For 190℃, they are 332 min, 528min, 835min and 1324min; for 210℃, they are 42 min, 66min, 105min and 167min; for 230℃, they are 21 min, 33min, 53min and 84min; for 250℃, they are 5 min, 8min, 13min and 21min. After each sample was taken at the reaction time, it was allowed to cool naturally to room temperature. Then, ethanol was added to each reaction solution (3:1 ratio) to remove excess surfactant. The mixture was then centrifuged to isolate the reaction product. The black reaction product was subsequently dispersed in 5ml hexanes. Samples for TEM characterization were prepared by dropping the hexanes suspension onto carbon-coated copper grids (Cu-200HD, Pacific Grid-Tech). When the hexanes suspension was dry, ethanol was utilized to rinse the TEM grid to remove excess surfactant.

The reaction of platinum ion reduction can be simply examined by observation of the color of the solution. At the beginning synthesis, the chemical solution presents yellow color induced by platinum ions. As reaction time increases, the nanoparticles start precipitating and present black color. As shown in Figure 5.5, the color of chemical solution changed from light yellow to black as reaction time increases at 250℃.

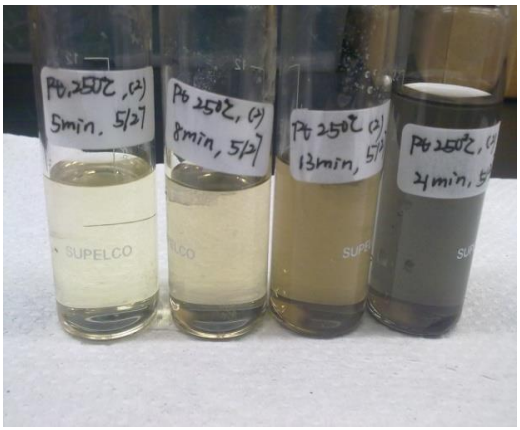

Figure 5.5: Color of chemical solution changed from light yellow to black as reaction time increases at 250℃.

5.4.3 TEM Analysis

The conventional bright field imaging and selected area diffraction patterns were carried out in a Philips EM420 transmission electron microscope operated at 120 kV. High-resolution transmission electron microscopy (HRTEM) and energy dispersive x-ray

spectroscopy (EDS) analysis were practiced in a FEI Titan 80-300 scanning/transmission electron microscope (S/TEM) operated at 300 kV. A typical setting for HRTEM imaging was a 70 um C2 aperture with an objective lens defocus of -58 nm.

References

[1] H. Lee, S.E. Habas, S. Kweskin, D. Butcher, G.A. Somorjai, P. Yang, Morphological control of catalytically active platinum nanocrystals, Angewandte Chemie-International Edition, 45 (2006) 7824-7828.

[2] A. Guerrero-Martinez, S. Barbosa, I. Pastoriza-Santos, L.M. Liz-Marzan, Nanostars shine bright for you Colloidal synthesis, properties and applications of branched metallic nanoparticles, Current Opinion in Colloid & Interface Science, 16 (2011) 118-127.

[3] C. Kim, J.-G. Oh, Y.-T. Kim, H. Kim, H. Lee, Platinum dendrites with controlled sizes for oxygen reduction reaction, Electrochemistry Communications, 12 (2010) 1596-1599.

[4] K.M. Yeo, S. Choi, R.M. Anisur, J. Kim, I.S. Lee, Surfactant-Free Platinum-on-Gold Nanodendrites with Enhanced Catalytic Performance for Oxygen Reduction, Angewandte Chemie-International Edition, 50 (2011) 745-748.

[5] H.-T. Zhang, J. Ding, G.-M. Chow, Morphological control of synthesis and anomalous magnetic properties of 3-D branched Pt nanoparticles, Langmuir, 24 (2008) 375-378.

[6] S. Guo, E. Wang, Noble metal nanomaterials: Controllable synthesis and application in fuel cells and analytical sensors, Nano Today, 6 (2011) 240-264.

[7] Z. Peng, H. Yang, Designer platinum nanoparticles: Control of shape, composition in alloy, nanostructure and electrocatalytic property, Nano Today, 4 (2009) 143-164.

[8] L. Wang, Y. Yamauchi, Synthesis of Mesoporous Pt Nanoparticles with Uniform Particle Size from Aqueous Surfactant Solutions toward Highly Active Electrocatalysts, Chemistry-a European Journal, 17 (2011) 8810-8815.

[9] A. Chen, P. Holt-Hindle, Platinum-Based Nanostructured Materials: Synthesis, Properties, and Applications, Chemical Reviews, 110 (2010) 3767-3804.

[10] K.A. Afanasyev, F. Sansoz, Strengthening in gold nanopillars with nanoscale twins, Nano Lett., 7 (2007) 2056-2062.

[11] R. Narayanan, M.A. El-Sayed, Shape-dependent catalytic activity of platinum nanoparticles in colloidal solution, Nano Letters, 4 (2004) 1343-1348.

[12] M. Sanles-Sobrido, M.A. Correa-Duarte, S. Carregal-Romero, B. Rodriguez-Gonzalez, R.A. Alvarez-Puebla, P. Herves, L.M. Liz-Marzan, Highly Catalytic Single-Crystal Dendritic Pt Nanostructures Supported on Carbon Nanotubes, Chemistry of Materials, 21 (2009) 1531-1535.

[13] J.Y. Chen, T. Herricks, M. Geissler, Y.N. Xia, Single-crystal nanowires of platinum can be synthesized by controlling the reaction rate of a polyol process, Journal of the American Chemical Society, 126 (2004) 10854-10855.

[14] F. Jia, F. Wang, Y. Lin, L. Zhang, Microwave-Induced Formation of Platinum Nanostructured Networks with Superior Electrochemical Activity and Stability, Chemistry-a European Journal, 17 (2011) 14603-14610.

[15] L. Wang, H. Wang, Y. Nemoto, Y. Yamauchi, Rapid and Efficient Synthesis of Platinum Nanodendrites with High Surface Area by Chemical Reduction with Formic Acid, Chemistry of Materials, 22 (2010) 2835-2841.

[16] H. Meng, F. Xie, J. Chen, S. Sun, P.K. Shen, Morphology controllable growth of Pt nanoparticles/nanowires on carbon powders and its application as novel electro-catalyst for methanol oxidation, Nanoscale, 3 (2011) 5041-5048.

[17] S. Sun, G. Zhang, Y. Zhong, H. Liu, R. Li, X. Zhou, X. Sun, Ultrathin single crystal Pt nanowires grown on N-doped carbon nanotubes, Chemical Communications, (2009) 7048-7050.

[18] A. Mohanty, N. Garg, R. Jin, A Universal Approach to the Synthesis of Noble Metal Nanodendrites and Their Catalytic Properties, Angewandte Chemie-International Edition, 49 (2010) 4962-4966.

[19] Y.J. Song, Y.B. Jiang, H.R. Wang, D.A. Pena, Y. Qiu, J.E. Miller, J.A. Shelnutt, Platinum nanodendrites, Nanotechnology, 17 (2006) 1300-1308.

[20] H.W. Shim, Y. Zhang, H. Huang, Twin formation during SiC nanowire synthesis, Journal of Applied Physics, 104 (2008).

[21] L. Vitos, A.V. Ruban, H.L. Skriver, J. Kollar, The surface energy of metals, Surface

Science, 411 (1998) 186-202.

[22] Z. Huo, C.-k. Tsung, W. Huang, X. Zhang, P. Yang, Sub-two nanometer single crystal Au nanowires, Nano Letters, 8 (2008) 2041-2044.

[23] C. Wang, S. Sun, Facile Synthesis of Ultrathin and Single-Crystalline Au Nanowires, Chemistry-an Asian Journal, 4 (2009) 1028-1034.

[24] L. Cademartiri, G.A. Ozin, Ultrathin Nanowires - A Materials Chemistry Perspective, Advanced Materials, 21 (2009) 1013-1020.

[25] X. Lu, M.S. Yavuz, H.-Y. Tuan, B.A. Korgel, Y. Xia, Ultrathin gold nanowires can be obtained by reducing polymeric strands of oleylamine-AuCl complexes formed via aurophilic interaction, Journal of the American Chemical Society, 130 (2008) 8900-+.

[26] L.-M. Lacroix, C. Gatel, R. Arenal, C. Garcia, S. Lachaize, T. Blon, B. Warot-Fonrose, E. Snoeck, B. Chaudret, G. Viau, Tuning Complex Shapes in Platinum Nanoparticles: From Cubic Dendrites to Fivefold Stars, Angewandte Chemie-International Edition, 51 (2012) 4690-4694.

Chapter 6

TEM Characterization of Pulsed Laser Deposition $BaTiO_3$ Film on Platinized Silicon

6.1 Background

BaTiO3 has tetragonal structure (c/a=1.01) at room temperature and it has ferroelectric property.[1, 2] Because of this unique ferroelectric property, BaTiO3 thin film has been extensively studied. [2, 3] The ferroelectric property of BaTiO3 is essentially crystallographic orientation dependent [2]; with the aim of high ferroelectric polarization, control of growth orientation of BaTiO3 thin film is desired. Besides the crystallographic orientation, the ferroelectric property also depends upon the crystal structure.[4-6] Defected structure can lead to failure of ferroelectric device such as ferroelectric random access memory. Therefore this chapter focuses on exploring the growth control and twin formation in BaTiO3 thin film. A $BaTiO_3$ film with columnar structures [3, 7, 8] was fabricated by pulsed laser deposition and characterized by TEM. The growth orientation of the thin film was found to be controlled by epitaxial growth of the substrate.[8, 9] Moreover the twin lamellae were found in the thin film and possible formation mechanisms of the twin lamellae are summarized in the end of this chapter.

6.2 Results and Discussion

In order to elucidate the preferred growth orientation and defect formation we explored the BaTiO3 film by TEM. Figure 6.1(a) shows a typical TEM bright field image of a cross-section $BaTiO_3$/Pt sample. The film has a well-developed columnar structure with a feather-like morphology growing along the vertical columnar boundary.[3, 8, 10] Like the flight feather, the columnar has a central stem (column) with array of barbs. To investigate the detailed atomic structure of both the columnar and barbs, a series of HRTEM images (Fig.

6.1(b) ~ (e)) were taken from the regions marked in Fig. 6.1(a). Although there are some local defects observed in the columnar structure, the general growth direction of the columnar structure and the barbs can be determined to be <111> and <110> from the FFT patterns, inset in Fig 6.1 (b) ~ (e). the columnar grains do not change their growth orientation while the thickness of column changes. In other words, the whole column grows along <111> orientation without any variation in the orientation.

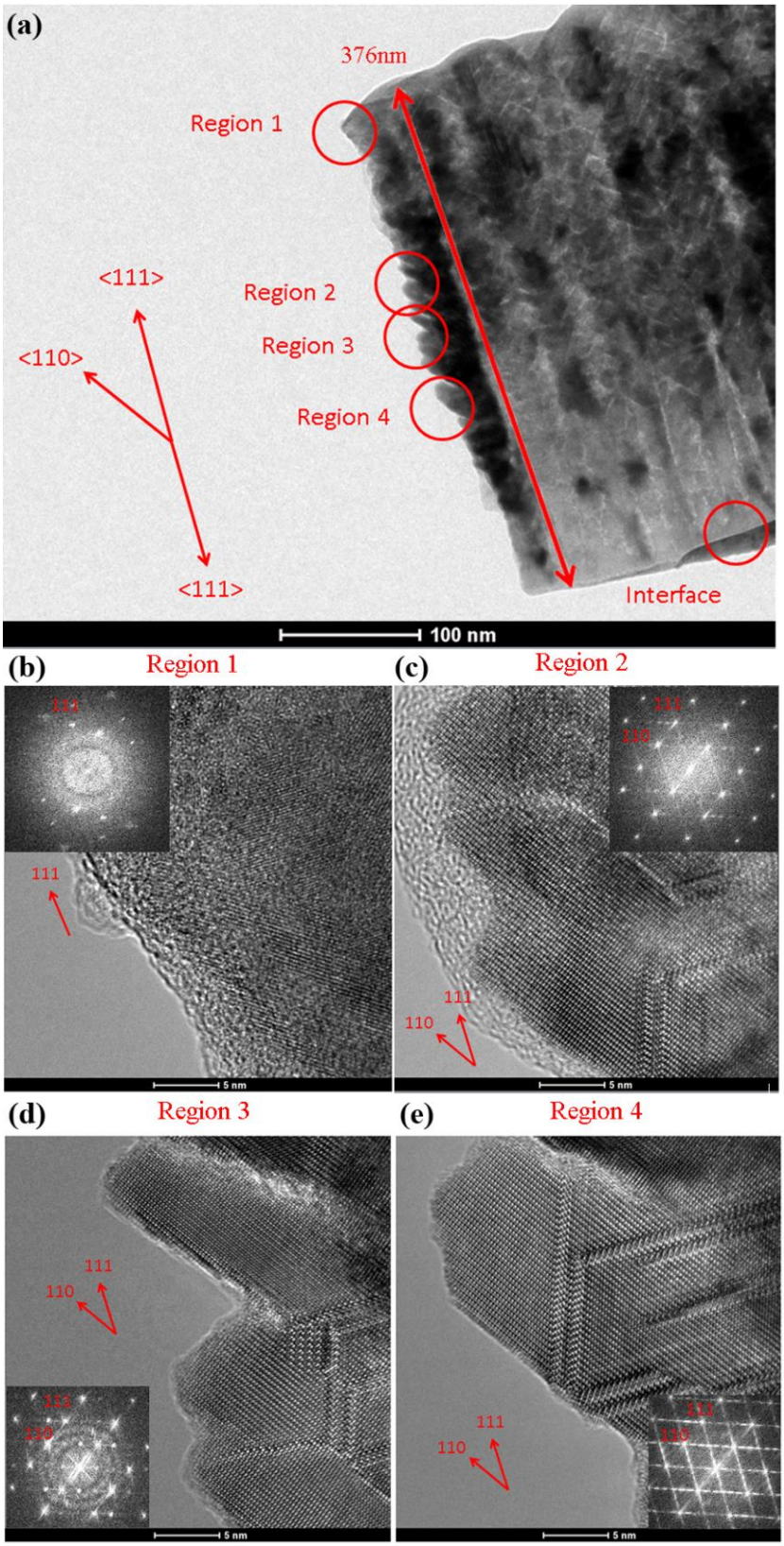

Figure 6.1: (a) TEM bright filed image of $BaTiO_3$ columnar structures on platinized silicon substrate. (b) ~ (e) refer to HRTEM images taken from "Region" denoted in (a).

There are planar defects distributed all across the central column and at the vicinity of

the barbs along the [111] axis in the majority of HRTEM images as shown in Fig 6.2 (a). These planar defects were identified to be Σ3 {111} twins by comparing the periodic structure of the planar defects in the HRTEM image to a simulated twinned structure as shown in Fig 6.2 (b).[5, 11] These twin lamellae often contain periodic twinned structure with fixed spacing.[1, 4]

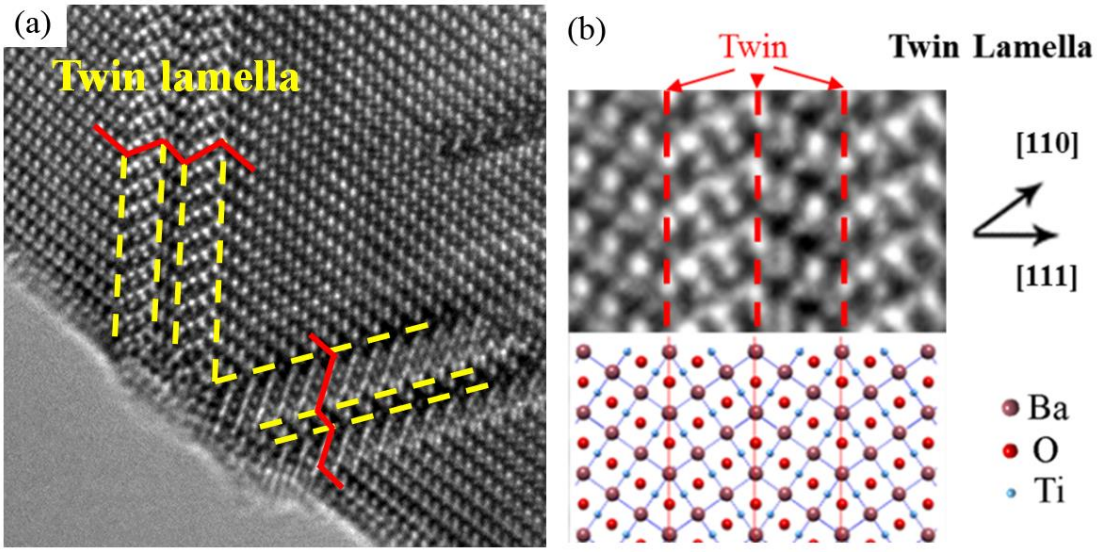

Figure 6.2: (a) HTEM image of twin lamellae in $BaTiO_3$ columnar structures. (b) Confirmation of experimental twin lamella structure with twin lamella simulated structure.

Meanwhile, Fig 6.3 illustrate HRTEM image of an "interface" region which denoted the interface between the $BaTiO_3$ film and Pt substrate in Figure 6.1 (a). The FFT patterns in Figure 6.3 confirm that majority of the $BaTiO_3$ film was grown epitaxially from the substrate along a <111> orientation.[8, 12]

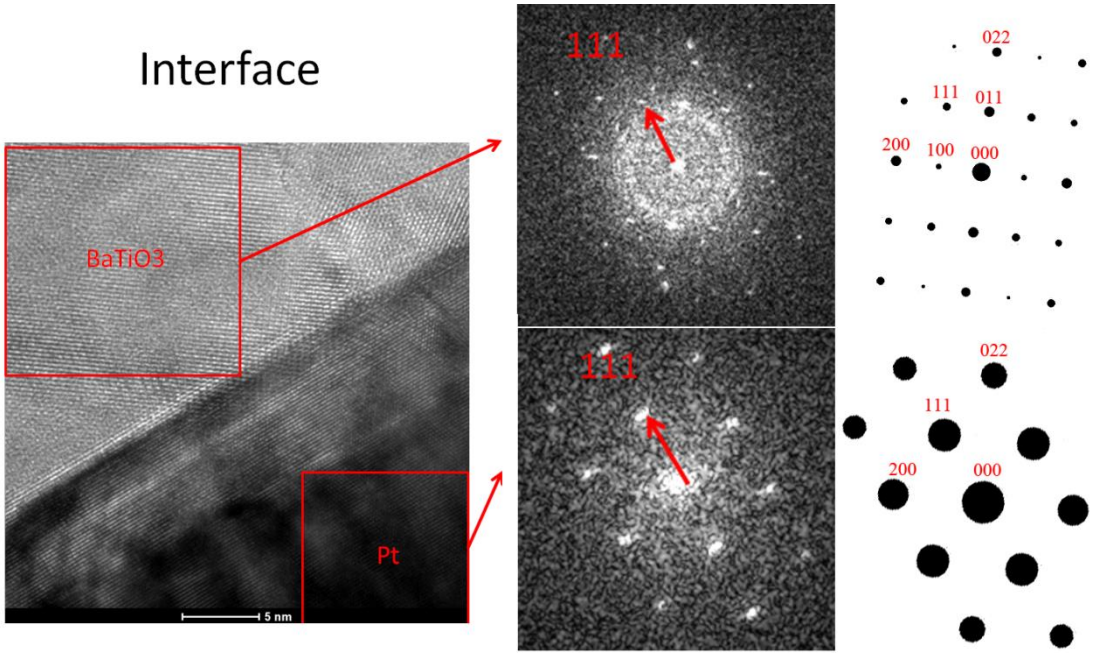

Figure 6.3: HTEM image of interface between $BaTiO_3$ film and Pt substrate. The FFTs represent the orientation relationship between $BaTiO_3$ film and Pt substrate. The majority of $BaTiO_3$ film grew epitaxially from the substrate along a <111> orientation.

My TEM study indicate that both columnar structures and barbs have preferred orientation and twin lamellae are widely distributed among them. Therefore, the reasons to the formation of twins and the control of growth orientation are interesting questions need to be answered. First of all, unlike other perovskite material such as $SrTiO_3$ and $CaTiO_3$, Σ3 {111} twin boundaries have been extensively observed in $BaTiO_3$ thin film with cubic and tetragonal structures.[1] Several explanations have been proposed for how twins are formed in the film. Jia et al. suggested that twin nucleation could occur from dissociation of a perfect <111> edge dislocation.[13] Jang et al. stated that both stacking fault and twin lamella can accommodate small misfit in the film.[12] Figure 6.4 (a) shows that regular $BaTiO_3$ cubic structure consist of TiO_6 structure; however, the Σ3 {111} twin boundary consist of Ti_2O_9 structure.[4] Therefore, a twin lamellar in cubic structure with fixed spacing between twin boundaries consist Ti_2O_9 structures (Figure 6.4 (b)) which are essential element of $BaTiO_3$ hexagonal structure (Figure 6.4 (c)).[11] This leads a twin lamella to have similar structure to $BaTiO_3$ hexagonal structure.[1, 14-16] Furthermore, it has been reported that $BaTiO_3$ hexagonal structure can exist under non-equilibrium condition.[12] Additionally, Zhu et al. show that

formation of twins is affected by the oxygen pressure of fabrication environment.[17] As the oxygen pressure decrease the density of nanotwins increases. [4, 18] It has been reported that in oxygen deficient environment, twins can accommodate the oxygen vacancies.[19]

The twin lamella observed in the columnar structure as shown in Figure 6.2 (b) has similar structure to $BaTiO_3$ hexagonal structure as shown in Figure 6.4 (c) Since the pulsed laser deposition in this experiment is a highly non-equilibrium process and the deposition occurred in a lack of oxygen environment (vacuum), it is highly possible that the formation of twin lamella in the columnar structures is due to the processing and the oxygen vacancies accommodation by twins.

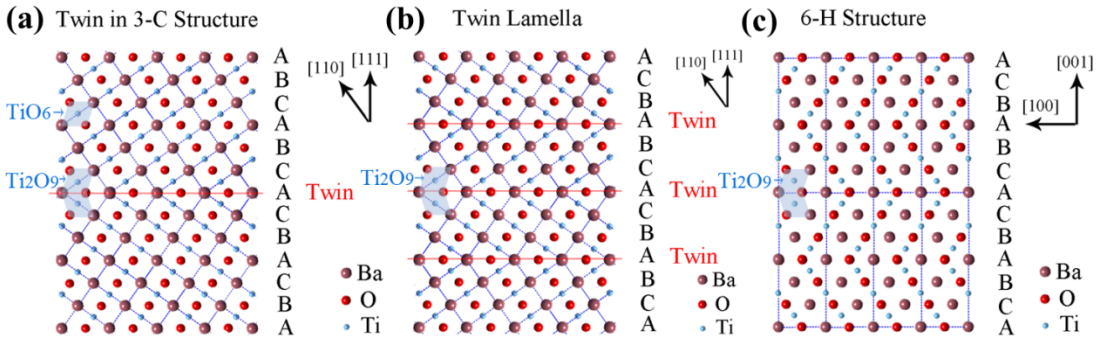

Figure 6.4: (a) A simulated $BaTiO_3$ 3-C structure with a twin boundary indicates that defect-free 3-C structure has TiO_6 structure; however, the structure at twin boundary has Ti_2O_9 structure. (b), a $BaTiO_3$ twin lamella in cubic structure with three {111} atomic d-spacing between twin boundaries, has similar structure to (c), $BaTiO_3$ hexagonal structure. Both structure consist Ti_2O_9 structures which are essential element of $BaTiO_3$ hexagonal structure

Next question needed to be addressed is control of preferred orientation. The FFT platinum substrate in the interface region indicates that the Pt substrate has preferred orientation of <111>. It is known that the lattice parameter of platinum is 0.392 nm and the lattice parameter of $BaTiO_3$ is 0.401nm.[3, 12] The lattice mismatch is only 2.1%. Therefore, to minimize the strain energy between the $BaTiO_3$ thin film and platinum substrate, $BaTiO_3$ thin film grew epitaxially from Pt substrate and this leads the preferred orientation of the thin film to a <111> orientation.[3, 8, 12]

6.3 Summary

In this chapter, I presented a collaboration work with Dr. S. Priya group (ME) studying $BaTiO_3$ thin film fabrication for energy harvesting device. My role in the investigation was to characterize the defected structure in $BaTiO_3$ thin film grown by pulsed laser deposition on platinized silicon substrate with transmission electron microscopy (TEM). The film has BaTiO3 poly-crystalline grains with columnar morphology grown in a <111> preferred orientation. The columnar grain consists of multiple twins. Thus, the ceramic columnar structure in this chapter shares similar morphology and structural characteristics with the metallic nanowires studied in the previous chapters. Here I present detailed TEM characterization of these columnar structures. The TEM result indicates that columnar structures were grown epitaxially from the substrate. The presence of twin lamellae which have similar structure to hexagonal $BaTiO_3$ can be due to lattice mismatch, dissociation of a perfect <111> edge dislocation, non-equilibrium processing and lack of oxygen environment.

6.4 Methods

6.4.1 Fabrication of BaTiO3 Film

BaTiO3 film was deposited on platinized silicon substrate by using KrF excimer pulsed laser deposition system (λ=248 nm). Stoichiometric BTO target were synthesized by conventional mixed-oxide processing route. During the deposition, the laser energy density, repetition rate and the oxygen pressure was kept at ~2.5 J/cm2, 10 Hz and 100mTorr respectively. The substrate temperature was maintained at 800 ° C during the whole deposition process.

6.4.2 TEM Analysis

High resolution transmission electron microscopy (HRTEM) was carried out in a FEI Titan 80-300 scanning/transmission electron microscope (S/TEM) operated at 300 kV. A typical imaging condition for HRTEM is defocus -58 nm with 70 m C2 aperture.

References

[1] E. Hamada, W.S. Cho, K. Takayanagi, Nanotwins in BaTiO3 nanocrystals, Philosophical Magazine a-Physics of Condensed Matter Structure Defects and Mechanical Properties, 77 (1998) 1301-1308.

[2] D.Y. Kim, S.G. Lee, Y.K. Park, S.J. Park, EFFECT OF AMBIENT GAS-PRESSURE ON THE PREFERRED ORIENTATION OF BARIUM-TITANATE THIN-FILMS PREPARED BY PULSED-LASER DEPOSITION, Japanese Journal of Applied Physics Part 2-Letters, 34 (1995) 1564-1566.

[3] D.Y. Kim, S.G. Lee, Y.K. Park, S.J. Park, Variation of the preferred orientation with thickness in barium titanate thin films prepared by pulsed laser deposition, Japanese Journal of Applied Physics Part 1-Regular Papers Brief Communications & Review Papers, 36 (1997) 7307-7311.

[4] Y.C. Wu, C.C. Lee, H.Y. Lu, D.E. McCauley, M.S.H. Chu, The {1(1)over-bar1} growth twins in tetragonal barium titanate, Journal of the American Ceramic Society, 89 (2006) 1679-1686.

[5] M. Fujimoto, Defects in epitaxially grown perovskite thin films, Journal of Crystal Growth, 237 (2002) 430-437.

[6] V. Krasevec, M. Drofenik, D. Kolar, GENESIS OF THE (111) TWIN IN BARIUM-TITANATE, Journal of the American Ceramic Society, 73 (1990) 856-860.

[7] J.A. Thornton, HIGH-RATE THICK-FILM GROWTH, Annual Review of Materials Science, 7 (1977) 239-260.

[8] D.Y. Kim, S.G. Lee, Y.K. Park, S.J. Park, Tailoring of the preferred orientation and microstructure in the deposition of BaTiO3 thin films using pulsed laser deposition, Materials Letters, 40 (1999) 146-150.

[9] C.H. Lei, C.L. Jia, M. Siegert, K. Urban, Investigation of {111} stacking faults and nanotwins in epitaxial BaTiO3 thin films by high-resolution transmission electron microscopy, Philosophical Magazine Letters, 80 (2000) 371-380.

[10] R.C. DeVries, Observations on Growth of BaTiO3, Crystals from KF Solutions, Journal of the American Ceramic Society, 42 (1959) 547-558.

[11] C.L. Jia, A. Thust, Investigation of atomic displacements at a Sigma 3 {111} twin boundary in BaTiO3 by means of phase-retrieval electron microscopy, Physical Review Letters, 82 (1999) 5052-5055.

[12] J.W. Jang, W.J. Cho, J.H. Lee, S.S. Choi, T.S. Hahn, Origin of (111) twin lamellae in BaTiO3 thin films on platinum substrates, Japanese Journal of Applied Physics Part 1-Regular Papers Short Notes & Review Papers, 36 (1997) 6942-6945.

[13] C.L. Jia, K. Urban, M. Mertin, S. Hoffmann, R. Waser, The structure and formation of nanotwins in BaTiO3 thin films, Philosophical Magazine a-Physics of Condensed Matter Structure Defects and Mechanical Properties, 77 (1998) 923-939.

[14] Y.C. Wu, H.Y. Lu, Crystallographic orientation relationships between hexagonal and tetragonal barium titanate, Journal of the American Ceramic Society, 88 (2005) 3154-3161.

[15] T. Watanabe, M. Shimada, T. Aiba, H. Yabuta, K. Miura, K. Oka, M. Azuma, S. Wada, N. Kumada, Structural Transformation of Hexagonal (0001)BaTiO3 Ceramics to Tetragonal (111)BaTiO3 Ceramics, Japanese Journal of Applied Physics, 50 (2011).

[16] Y.-C. Wu, S.-F. Wang, H.-Y. Lu, Stacking faults and stacking fault energy of hexagonal barium titanate, Journal of the American Ceramic Society, 89 (2006) 3778-3787.

[17] Y.L. Zhu, S.J. Zheng, D. Chen, X.L. Ma, Microstructure tuning of epitaxial BaTiO3 (-) (x) thin films grown using laser molecular-beam epitaxy by varying the oxygen pressure, Thin Solid Films, 518 (2010) 3669-3673.

[18] K.P. Fahey, B.M. Clemens, L.A. Wills, NONORTHOGONAL TWINNING IN THIN-FILM OXIDE PEROVSKITES, Applied Physics Letters, 67 (1995) 2480-2482.

[19] C.L. Jia, K. Urban, Atomic-resolution measurement of oxygen concentration in oxide materials, Science, 303 (2004) 2001-2004.

Chapter 7
Conclusions and Suggestions for Future Works

7.1 Conclusions

The conclusions of this dissertation are listed as follows.

1. We have developed a plausible explanation for twinning and twinning superlattices found in <111>- oriented ultrathin gold nanowires. Our model demonstrates that the relative values of a material dependent factor, φ , and a shape dependent factor *S* can explain the presence or absence of twins in gold and platinum nanowires. Considerations of twinning formation within this thermodynamic framework may have implications for control of twinning in multiple nanomaterials.
2. We have presented a stereo vision technique for achieving atomic resolution 3D reconstruction in crystalline nanoparticles tens of nanometers in size that does not rely upon an assumed structural model or scattering intensity distributions to estimate atomic arrangements in the projection direction. By taking {111} atomic planes (epipolar planes) as references, 2D images can be aligned to atomic scale accuracy The method can provide some 3D structural details about crystalline defects such as dislocations and crystal boundaries.
3. The software tool, AutoSADP, and an associated suite of programs that automates the analysis of diffraction patterns were described. The algorithm in the AutoSADP tool locates both the forward scattered beam and diffraction spots automatically and accurately. Both analysis of simulated diffraction spots and experimental SADPs demonstrate that the detected locations are accurate to within typical precision of experimental diffraction patterns. For real diffraction patterns, the errors are less than 0.5% for the ratio of reciprocal vectors and 1.89% for interplanar angles. These errors are well enough for indexing the diffraction spots [7]. The AutoSADP algorithm works well on non centrosymmetric patterns, diffraction patterns with high noise (like FFTs), and diffraction patterns with streaked diffraction spots.

4. We demonstrated that the morphology of platinum nanocrystals (nanodendrites, nanoflowers and nanowires) can be controlled by reaction time and temperature in a one-pot chemical synthesis method. Additionally, we present a fitted Arrhenius equation to predict the growth rate of platinum nanowires by reaction temperature.

7.2 Suggestions for Future Works

1. It has been reported that the spacing between twin boundaries in Indium phosphide nanowires fabricated by vapor solid liquid method is a function of the diameter of the nanowires. The thickness of our gold nanowires is not monodisperse; therefore, the spacing between twin boundaries can possibly be affected by the fluctuation of nanowire thickness. Thus, it would be interesting to investigate the spacing between twin boundaries in monodisperse gold nanowires.
2. Our geometric model explains the formation of twinning in <111>- oriented nanowires fabricated by solution-phase chemical synthesis method in gold and platinum systems. It would be interesting to investigate other fcc systems such as nickel, copper and aluminum. Especially aluminum, it has been reported that even it has low stacking fault energy comparing to nickel it has lower tendency to form deformation twinning is bulk materials.
3. The newly developed stereo vision 3D reconstruction technique can successfully reconstruct 3D atomic structure of a nanowire in fcc system which has high crystal symmetry. It would be interesting to apply our method in more complex crystal structure system such as triclinic.